



Exploring Dynamic Enhancements in MHD Heat Transfer with Second Order Slip Model in Radiative Fluid Flow Through Porous Media along a Stretching Cylinder



Purnima Rai* , Upendra Mishra 

Department of Mathematics, Amity University Rajasthan, Rajasthan 303002, India

Corresponding Author Email: purnima.rai411@gmail.com

Copyright: ©2024 The authors. This article is published by IIETA and is licensed under the CC BY 4.0 license (<http://creativecommons.org/licenses/by/4.0/>).

<https://doi.org/10.18280/ijht.420324>

ABSTRACT

Received: 12 February 2024

Revised: 22 March 2024

Accepted: 1 April 2024

Available online: 27 June 2024

Keywords:

stretching cylinder, radiation, second order slip, porous medium, finite element method

This study explores the complex dynamics of magnetohydrodynamic (MHD) flow within a porous medium while considering the impact of thermal radiation. The primary focus of the investigation centers on a cylinder that is vertically elongating, serving as a means to characterize the behavior of a viscous, incompressible fluid. Notably, the analysis introduces an added layer of intricacy by incorporating both second-order momentum slip and first-order thermal slip boundary conditions. By applying well-suited similarity variables, the governing equations encompassing continuity, momentum, and energy are transformed into a set of non-linear ordinary differential equations. The method employed to effectively handle these equations is the finite element method, known for its robustness in numerical approaches. This approach facilitates the exploration of detailed insights into the distribution of velocity and temperature, consequently revealing nuanced patterns and prevailing trends. A thorough examination of diverse physical parameters offers a comprehensive understanding of their respective influences, thus providing a holistic perspective on their roles within the system. The research goes on to present explicit formulations for critical parameters, including the skin-friction coefficient, Nusselt number, fluid velocity, and temperature surrounding the cylinder. These formulations are visually elucidated through informative graphical depictions. Beyond its theoretical contributions, this research carries tangible practical significance across domains such as thermal engineering, fluid dynamics, and energy systems. Its insights have the potential to impact the optimization and design of real-world processes and systems, underscoring its relevance to technological advancements in these fields.

1. INTRODUCTION

Over the years, researchers have delved into the fascinating field of magnetohydrodynamics (MHD) and its significant applications in fluid dynamics across various industries, including metallurgy, materials processing, chemical engineering, and environmental processes. A captivating area of investigation has been the impact of MHD on heat transfer in fluid flow along a stretching cylinder, particularly in the presence of porous media and radiative effects.

Numerous studies have explored the influence of MHD in different scenarios. Ganesan and Loganathan [1] examined the effects of a magnetic field on a vertical cylinder with a constant heat flux, while Ishak et al. [2] focused on MHD flow and heat transfer around a stretching cylinder. Chamkha [3] ventured into heat and mass transfer under the influence of MHD flow over a moving permeable cylinder, considering heat generation, absorption, and chemical reactions. In the context of porous media, Makanda et al. [4] investigated the role of radiation on MHD free convection from a horizontal circular cylinder with partial slip in a non-Darcy porous medium, including viscous dissipation. Similarly, Malik and Salahuddin [5] explored MHD stagnation point flow of the Williamson fluid model over a stretching cylinder.

Additionally, researchers like Hayat et al. [6] studied the intriguing interplay of thermal radiation and magnetic field in the boundary layer flow of a viscous fluid around a nonlinear stretching cylinder. On a related note, Mondal et al. [7] explored the influence of an inclined stretching cylinder on MHD mixed convective nanofluid flow, incorporating chemical reactions and viscous dissipation.

These diverse investigations have illuminated the complex phenomena of second-order slip and MHD effects on heat transfer in boundary layer flow around cylinders. The findings hold practical implications in various engineering applications, materials science, aerodynamics, nanotechnology, and energy systems. As researchers continue to build upon this knowledge, further advancements in understanding and applying MHD in fluid dynamics are expected to drive innovation in numerous industrial sectors.

The exploration of boundary layer flow around cylinders with radiation has garnered substantial interest due to its significant industrial implications. Noteworthy studies include Yih [8], who explored the impact of radiation on natural convection around an isothermal vertical cylinder embedded in a saturated porous medium. Additionally, Soid et al. [9] conducted an analysis of laminar boundary layer flow along a stretching cylinder with thermal radiation. Additionally, Najib

and Bachok [10] conducted an analysis of laminar boundary layer flow along a stretching cylinder with thermal radiation. Similarly, Chauhan et al. [11] investigated stagnation point flow and mass transfer with chemical reactions past a stretching/shrinking cylinder, accounting for natural convection and thermal radiation effects. Moreover, Pandey and Kumar [12] focused on MHD flow and heat transfer outside a hollow stretching cylinder immersed in a fluid-saturated highly porous medium, considering the influence of radiation. Likewise, Shojaei et al. [13] studied the combined influence of thermal radiation and viscous dissipation on nanofluid flow over a stretching cylinder in a porous medium. Additionally, Lim et al. [14] performed a hydrothermal analysis of non-Newtonian second-grade fluid flow on a radiative stretching cylinder, considering Soret and Dufour effects. Furthermore, Abbas et al. [15] explored the impact of chemical reaction, thermal radiation, and porosity on free convection Carreau fluid flow around a stretching cylinder. Moreover, Jarwal et al. [16] delved into the thermodynamics of radiative, chemically reactive flow of induced MHD Sutter by nanofluid over a nonlinear stretching cylinder. Recently, Wang and Ng [16] investigated the effect of thermal radiation on mixed convection boundary layer MHD flow of nanofluid through a porous stretching cylinder. These diverse research endeavors have provided valuable insights into the intricate interactions of radiation, magnetic forces, chemical reactions, and porous media in heat transfer phenomena around cylinders, with practical applications in engineering, materials science, nanotechnology, and energy systems.

Another intriguing area of investigation concerns the boundary layer flow with slip effects around a stretching cylinder, which holds significant industrial applications. Various researchers have made notable contributions in this area. Wang and Ng [17] examined slip-rarefied flow due to a stretching cylinder, while Fang et al. [18] provided solutions for viscous flow over a shrinking cylinder using a proposed second-order slip flow model. Zhu et al. [19] investigated steady boundary layer flow and heat transfer near the forward stagnation point of plane and axisymmetric sheet towards a stretching sheet with velocity slip and temperature jump. Additionally, Mukhopadhyay [20] conducted a study on MHD boundary layer slip flow along a stretching cylinder, and Mishra and Singh [21] investigated dual solutions of mixed convection flow with momentum and thermal slip flow over a permeable shrinking cylinder. Dhanai et al. [22] explored MHD mixed convection nanofluid flow and heat transfer over an inclined cylinder with velocity and thermal slip effects, while Jain and Bohra [23] focused on entropy generation in magnetohydrodynamic fluid flow and heat transfer over a stretching cylinder with a porous medium in the slip flow regime. Lastly, Soomro et al. [24] studied the characteristics of mixed convection flow with heat transfer of nanofluid along a porous shrinking cylinder with slip effects. These comprehensive research efforts have shed light on slip-rarefied flow phenomena and their implications in heat transfer processes, providing valuable insights for applications in various industrial sectors.

The study of porous medium-mixed convection boundary layer flow along a stretching cylinder also holds significant industrial applications. Researchers like Mukhopadhyay [25] have explored this phenomenon, Rashad et al. [26] focused on studying mixed convection boundary-layer flow past a horizontal circular cylinder embedded in a porous medium filled with a nanofluid under convective boundary conditions.

EL-Kabeir et al. [27] delved into the effects of thermal radiation and nonlinear Forchheimer terms on boundary-layer flow and heat transfer from a vertical cylinder embedded in a porous medium saturated with nanofluids, providing valuable insights. Similarly, Yadav and Sharma [28] investigated MHD fluid flow and heat transfer characteristics of a viscous incompressible fluid along a continuously stretching horizontal cylinder embedded in a porous medium. Notably, Manjunatha et al. [29] developed a numerical analysis to study the flow and velocity characteristics of an electrically conducting dusty fluid over a stretching cylinder in the presence of a transverse magnetic field and thermal radiation, further contributing to the understanding of this complex phenomenon. Alizadeh et al. [30] explored mixed convection and thermodynamic irreversibilities in MHD nanofluid stagnation-point flows over a cylinder embedded in porous media. Finally, Dharmendar Reddy et al. [31] investigated the impact of heat absorption/generation on MHD heat transfer fluid flow along a stretching cylinder with a porous medium, providing valuable insights for practical applications in various industrial sectors. These research studies have collectively enriched our understanding of the intricate flow and heat transfer phenomena occurring in porous media around stretching cylinders, with practical implications in diverse industrial applications.

Additionally, the study of fluid flow along a stretching cylinder has numerous industrial applications. Merkin et al. [32] focused on studying the stagnation-point boundary-layer flow and heat transfer over an exponentially stretching/shrinking cylinder, contributing to the understanding of this complex flow behavior. Awaludin et al. [33] conducted a study on the steady flow over a permeable shrinking horizontal cylinder with a prescribed surface heat flux, shedding light on the heat transfer characteristics in such systems. Moreover, Najib et al. [34] explored the movement of viscous fluid and heat transfer rate when the cylinder shrinks, adding to the knowledge in this field. These research studies have collectively enhanced our understanding of fluid flow and heat transfer phenomena around stretching and shrinking cylinders, with potential practical applications across various industrial sectors.

Numerical methods play a crucial role in solving the complex boundary layer equations encountered in fluid flow and heat transfer problems. Various researchers have employed different numerical techniques to tackle these challenges. Yih [8] used an implicit finite-difference method, specifically the Keller box method, to solve the boundary layer equations. Ganesan and Loganathan [1] employed a finite difference scheme of Crank-Nicolson type to solve the governing equations for flow and heat transfer. Ishak et al. [2] utilized a similarity transformation followed by the Keller-box method for numerical solutions. Najib et al. [10] applied a shooting method to handle the transformed equations numerically. Chamkha [3] adopted a standard fully implicit, iterative, tri-diagonal finite-difference method to numerically solve the equations. Rashad et al. [26] used an efficient implicit, iterative, finite-difference method for the numerical solution. Mishra and Singh [21] used the Runge-Kutta Fehlberg method with a shooting technique. Merkin et al. [32] also applied a shooting method to handle ordinary differential equations numerically. EL-Kabeir et al. [27] employed an efficient implicit finite-difference method, while Manjunatha et al. [29] used the efficient Runge-Kutta Fehlberg-45 method due to the highly nonlinear and coupled nature of the

equations. Dhanai et al. [22] employed the fourth-order Runge-Kutta-Fehlberg method with a shooting technique for numerical solutions. Jain and Bohra [23] utilized the fourth-order Runge-Kutta scheme together with the shooting method to obtain numerical solutions for the set of nonlinear ordinary differential equations. Soomro et al. [24] sought numerical solutions using the Finite Difference Method (FDM) for the governing ODEs. Alizadeh et al. [30] and Rai and Mishra [35] solved the model using a finite difference scheme. Lim et al. [14] employed the optimal homotopy analysis method to solve the transformed highly nonlinear governing equations. Rai and Mishra [36]. Lastly, Dharmendar Reddy et al. [31] used similarity variables and the Keller-Box approach to numerically solve the ODEs. Additionally, Rai and Mishra [36] and Rai and Mishra [37] utilized the Finite Element Method to study boundary layer flow, underscoring its effectiveness and precision in handling complex flow phenomena.

After a comprehensive review of various numerical methods, the Finite Element Method (FEM) emerged as the preferred choice for our study due to its versatility and efficacy in handling complex geometries and boundary conditions. Unlike finite difference schemes, which often discretize domains with uniform grids, FEM's flexible meshing capability allows for precise representation of irregular shapes and boundaries, essential for accurately modeling the fluid dynamics around a stretching cylinder. The higher-order approximation offered by FEM ensures more accurate solutions while requiring fewer computational nodes, thereby reducing computational costs. Additionally, FEM's adeptness in managing mixed boundary conditions and diverse governing equations aligns seamlessly with the intricate nature of our study, which encompasses interactions between MHD effects, second-order slip dynamics, and radiative heat transfer. Its capacity to handle coupled equations and nonlinearities further enhances its suitability for simulating the complex fluid flow phenomena encountered in our research. Leveraging FEM, we aim to attain precise and robust numerical solutions, thereby advancing our understanding of fluid systems around stretching cylinders and contributing valuable insights to the field of fluid dynamics research.

Our research presents a novel exploration into the dynamics of magnetohydrodynamic (MHD) heat transfer with a second-order slip model, focusing on fluid flow along a stretching cylinder. The significance of our study lies in its comprehensive investigation of the interplay between MHD effects, second-order slip dynamics, and radiative heat transfer within a porous medium. Specifically, we address a notable gap in the literature by pioneering the application of the Finite Element Method (FEM) to study second-order slip effects in MHD heat transfer scenarios, offering insights beyond the scope of previous studies that primarily relied on finite difference methods and other numerical techniques. By leveraging FEM's capabilities to handle complex geometries, mixed boundary conditions, and higher-order approximations, our research contributes to advancing the understanding of fluid flow phenomena and thermal behavior, with practical implications for optimizing processes in industrial sectors and enhancing energy efficiency.

2. FORMULATION OF PROBLEM

This research focuses on studying the characteristics of

axisymmetric mixed convection flow involving a viscous incompressible fluid around an infinite, permeable stretching vertical cylinder with a fixed radius 'a' as shown in Figure 1.

To facilitate the analysis, several assumptions are made to simplify the model:

- The problem is approached using a coordinate system consisting of cylindrical coordinates (x, r), where x corresponds to the direction along the vertical axis of the cylinder, and r represents the radial direction. A homogeneous magnetic field acts radially in the system.
- The cylinder undergoes with a stretching velocity described by $U_w(x) = U_0 \left(\frac{x}{l}\right)^n$, while the prescribed surface temperature $(x) = T_\infty + T_0 \left(\frac{x}{l}\right)^n$, In the case of forced convection. 'n' represents the temperature exponent. n is the Temperature exponent, n is chosen, with n = 1 being utilized for mixed convection situations. The parameters U_0 and T_0 stand for the reference velocity and temperature, respectively, and L represents the characteristic length.
- In the present setup, a uniform magnetic field characterized by intensity B_0 is imposed in the radial direction, as depicted in Figure 1. Notably, when dealing with small magnetic Reynolds numbers, it is assumed that the effect of the induced magnetic field can be disregarded or considered negligible.
- In this study, the surface of the stretching cylinder is set at a constant temperature, T_w , which is higher than the ambient fluid temperature, T_∞ .
- To comprehensively examine the system, the influence of thermal radiation is considered. The radiative fluid is characterized as gray, indicating that it emits and absorbs radiation but does not scatter it. The thermal radiation is unidirectional, flowing transversely to the stretching cylinder. Moreover, throughout the analysis, the assumption is made that both the fluid and the porous medium are in local thermal equilibrium.

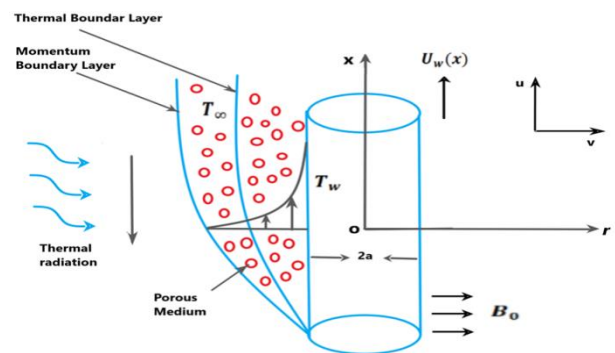


Figure 1. Diagrammatic illustration

The governing equations for continuity, momentum, and energy, considering boundary layer flow and the Boussinesq approximation, can be expressed as follows:

$$\frac{\partial}{\partial x}(ru) + \frac{\partial}{\partial y}(rv) = 0 \quad (1)$$

$$u \frac{\partial u}{\partial x} + v \frac{\partial u}{\partial r} = \frac{v}{r} \frac{\partial}{\partial r} \left(r \frac{\partial u}{\partial r} \right) - \frac{\sigma B_0^2}{\rho} u - \frac{v}{\kappa_p} u + g\beta(T - T_\infty) \quad (2)$$

$$\frac{\partial T}{\partial x} + v \frac{\partial T}{\partial r} = \frac{\alpha}{r} \frac{\partial}{\partial r} \left(r \frac{\partial T}{\partial r} \right) + \frac{Q}{\rho C_p} (T - T_\infty) - \frac{1}{\rho C_p} \frac{\partial q_r}{\partial y} \quad (3)$$

The components of velocity in the x and r directions are denoted by u and v , respectively. Here, $\nu = \frac{\mu}{\rho}$ represents the kinematic viscosity, calculated as the product of the coefficient of fluid viscosity μ and the fluid density ρ . Additionally, σ signifies the electrical conductivity of the medium, and B_0 represents the magnitude of the uniform magnetic field. The thermal diffusivity of the fluid is represented by α , while T represents the fluid temperature. The acceleration due to gravity is denoted by g , and the volumetric coefficient of thermal expansion is represented by β . The q_r represents the radiation heat flux, and κ_p denotes the permeability of the medium.

The appropriate boundary conditions for the problem are as follows:

$$r = a; u = U_w(x) = a_1 \frac{\partial u}{\partial r} + b_1 \frac{\partial^2 u}{\partial r^2}, T = T_w(x) + c_1 \frac{\partial T}{\partial r} \quad (4)$$

$$r \rightarrow \infty: u \rightarrow U_\infty, \quad T \rightarrow T_\infty, \quad C \rightarrow C_\infty,$$

The Boundary condition involves wall mass transfer velocity, $v_w(x)$, where a_1 and b_1 represent the first and second-order slip coefficients, respectively. Additionally, the thermal slip/jump coefficient is denoted by c_1 . These coefficients play a crucial role in characterizing the slip effects and thermal behavior at the fluid-solid interface.

According to the Rosseland diffusion approximation, the radiative heat flux is given by q_r .

$$q_r = \frac{4\sigma^*}{3k^*} \frac{\partial T^4}{\partial y} \quad (5)$$

where, σ^* and k^* are the Stefan-Boltzmann constant and the Rosseland mean absorption, Coefficient, respectively. We assume that the temperature differences within the flow are sufficiently small so that T^4 may be expressed as a linear function of temperature.

$$T^4 \approx 4 T_\infty^3 T - 3 T_\infty^4 \quad (6)$$

Using (5) and (6) in Eq. (3), we obtain:

$$\frac{\partial q_r}{\partial y} = - \frac{16 \sigma^* T_\infty^3}{3k^*} \frac{\partial^2 T^4}{\partial y^2} \quad (7)$$

By introducing the appropriate similarity variables [18, 20, 24, 30], Eqs. (1) - (3) can be simplified and reduced to ordinary differential equations (ODEs):

$$\eta = \frac{r^2 - a^2}{2r_0} \sqrt{\frac{U_w(x)}{vx}}, \psi = \sqrt{U_w(x)vx} af(\eta), \quad (8)$$

$$u = \frac{1}{r} \frac{\partial \psi}{\partial r}, v = - \frac{1}{r} \frac{\partial \psi}{\partial x}, \quad \theta(\eta) = \frac{T - T_\infty}{T_w - T_\infty}$$

In this context, the similarity variable is represented by η , and the stream function is represented by ψ . The dimensionless stream function is introduced as $f(\eta)$, and the dimensionless fluid temperature is denoted by $\theta(\eta)$. The utilization of these dimensionless functions allows us to simplify the governing equations and analyze the problem in a more convenient and concise manner.

The expression of velocity can be described by the following forms:

$$u = U_0 x f'(\eta) \text{ and } v = - \frac{a}{r} \sqrt{U_0} v f(\eta) \quad (9)$$

By employing the aforementioned transformations, Eqs. (2) and (3), along with the specified boundary conditions (4), can be expressed in the following form:

$$(1 + 2\eta\gamma) f'''' - (f')^2 + ff'' + 2\gamma f'' - (M + k)f' + Gr\theta = 0 \quad (10)$$

$$(1 + 2\eta\gamma)(3R + 4)\theta'' + 2\gamma\theta' + Pr(f\theta' - f'\theta) = 0 \quad (11)$$

The boundary constraints (4) can be simplified to the following expressions:

$$\eta = 0: f(0) = \xi, f'(0) = -1 + \lambda_1 f''(0) + \lambda_2 f'''(0), \theta(0) = 1 + \delta \theta'(0) \quad (12)$$

$$\eta \rightarrow \infty: f'(\infty) = 0, \theta(\infty) = 0$$

Table 1. Compilation of physical parameters and corresponding mathematical expressions

Parameter	Symbol	Expression	Parameter	Symbol	Expression
Transverse Curvature	γ	$\gamma = \sqrt{\frac{v}{U_0 a^2}}$	Permeability parameter	k	$k = \frac{v}{U_0} \kappa_p$
Grashof number	Gr	$Gr = \frac{g\beta(T_w - T_\infty) x^3}{\nu^2}$	Magnetic Parameter	M	$M = \sqrt{\frac{\sigma B_0^2}{\rho U_0}}$
Reynolds Number	Re	$Re = \frac{(U_0 x)x}{\nu}$	First order slip velocity parameter	λ_1	$\lambda_1 = (a_1 + b_1) \sqrt{\frac{U_0}{v}}$
Buoyancy parameter	B_y	$B_y = \frac{g\beta(T_w - T_\infty)}{U_0^2 x} = \frac{Gr}{Re^2}$	Second order slip velocity parameter	λ_2	$\lambda_2 = b_1 \sqrt{\frac{U_0}{v}}$
Prandtl number	Pr	$Pr = \frac{\nu}{\alpha}$	Thermal slip parameter	δ	$\delta = c_1 \sqrt{\frac{U_0}{v}}$
Radiation parameter	R	$R = \frac{k^* K}{4\sigma^* T_\infty^3}$	Wall mass transfer parameter	ξ	$\xi = -v_w(x) \sqrt{\frac{1}{U_0 v}}$

In the above equations, we encounter several parameters that play significant roles in characterizing the system. These parameters are summarized in the Table 1.

These parameters play a significant role in characterizing the behavior of the system and its sensitivity to changes in fluid properties, geometry, and flow conditions. An interesting observation is that $\gamma = \sqrt{\frac{\nu}{U_0 a^2}} = \frac{(\nu/U_0)^{1/2}}{a}$ and when $a \rightarrow 1$, implying γ approaches 0.

In accordance with the studies by Fang et al. and Zhu et al. and Mishra et al., we consider the parameters $\lambda_1 > 0$, $\lambda_2 < 0$, and $\delta > 0$, respectively. Furthermore, in the current problem, the parameter s is taken as positive, as this condition ensures that the flow remains laminar, and the vorticity is confined within the boundary layer.

The Eqs. (6) and (7), along with boundary conditions (8), are solved using the numerical finite element method. After obtaining the values of $f''(0)$, they are cross-checked and compared with the corresponding values given in Table 2. The favorable comparisons serve as strong evidence to support the reliability and effectiveness of the selected numerical scheme. The skin-friction coefficient at the surface of the cylinder is expressed as follows:

$$\eta \frac{1}{2} \sqrt{Re C_f} = f''(0) \quad (13)$$

The rate of heat transfer in terms of the Nusselt number at the surface of the cylinder is represented by the following expression:

$$\frac{Nu}{\sqrt{Re}} = -\theta'(0) \quad (14)$$

Table 2. Comparing the numerical values of $f''(0)$ with previously published results when $\lambda_1 = 0.5$, $\xi = 2.0$, $B_y = \gamma = R = k = M = 0$

λ_2	Fang et al. [18]	Mishra et al. [20] First Solution	Present Results
-1.0	0.341159	0.34121	0.34171
-2.0	0.20377	0.20382	0.20417

3. METHOD OF SOLUTION

First of all rewriting Eqs. (10) and (11), that is making coefficient of highest derivative equal to (10) and renaming these equations as (15)-(17).

$$f''' - \frac{1}{1+2\eta\gamma}(f')^2 + \frac{1}{1+2\eta\gamma}ff'' + \frac{2\gamma}{1+2\eta\gamma}f'' - \frac{M+k}{1+2\eta\gamma}f' + \frac{Gr}{1+2\eta\gamma}\theta = 0 \quad (15)$$

$$\theta'' + \frac{2\gamma}{(1+2\eta\gamma)(3R+4)}\theta' + \frac{Pr}{(1+2\eta\gamma)(3R+4)}(f\theta' - n f'\theta) = 0 \quad (16)$$

Along with the boundary conditions

$$\begin{cases} \eta = 0 : f(0) = \xi, f'(0) = -1 + \lambda f''(0) \\ \quad + \delta f'''(0), \theta(0) = 1 + \varepsilon \theta'(0) \\ \eta \rightarrow \infty : f'(\infty) = 0, \theta(\infty) = 0 \end{cases} \quad (17)$$

We will convert third order differential equation by replacing $F = f'$ in Eqs. (15) to (17), Then these equations will become as:

$$f' = F \quad (18)$$

$$F'' - \frac{1}{1+2\eta\gamma}F^2 + \frac{1}{1+2\eta\gamma}fF' + \frac{2\gamma}{1+2\eta\gamma}F' - \frac{M+K}{1+2\eta\gamma}F + \frac{Gr}{1+2\eta\gamma}\theta = 0 \quad (19)$$

$$\theta'' + \frac{2\gamma}{(1+2\eta\gamma)(3R+4)}\theta' + \frac{Pr}{(1+2\eta\gamma)(3R+4)}(f\theta' - nF\theta) = 0 \quad (20)$$

Corresponding boundary conditions will become as:

$$\begin{cases} \eta = 0, & f(0) = \xi, \\ & F(0) = -1 + \lambda_1 F'(0) + \lambda_2 F''(0), \\ & \theta(0) = 1 + \beta \theta'(0) \\ \eta = \infty, & \eta \rightarrow \infty : F(\infty) = 0, \theta(\infty) = 0 \end{cases} \quad (21)$$

Eq. (9) is nonlinear in variable F , which needs to be linearized, for this we will use the following method to make them linear. (making linear with respect to variable F).

$$F'' - \frac{1}{1+2\eta\gamma}F^2 + \frac{1}{1+2\eta\gamma}fF' + \frac{2\gamma}{1+2\eta\gamma}F' - \frac{M+K}{1+2\eta\gamma}F + \frac{Gr}{1+2\eta\gamma}\theta = 0, F(0) = -1 + \lambda_1 F'(0) + \lambda_2 F''(0), \theta(0) = 1 + \beta \theta'(0) \quad (22)$$

$$\eta = \infty, \quad \eta \rightarrow \infty : F(\infty) = 0, \theta(\infty) = 0$$

$$F'' = \frac{1}{1+2\eta\gamma}F^2 - \frac{1}{1+2\eta\gamma}fF' - \frac{2\gamma}{1+2\eta\gamma}F' + \frac{M+K}{1+2\eta\gamma}F - \frac{Gr}{1+2\eta\gamma}\theta \quad (23)$$

In the above equation, let $h(\eta, F, F')$ in the right hand side of above equation.

$$h(\eta, F, F') = \frac{1}{1+2\eta\gamma}F^2 - \frac{1}{1+2\eta\gamma}fF' - \frac{2\gamma}{1+2\eta\gamma}F' + \frac{M+K}{1+2\eta\gamma}F - \frac{Gr}{1+2\eta\gamma}\theta \quad (24)$$

Now,

$$A_k = -\left(\frac{\partial h}{\partial F'}\right)_k = -\left[-\frac{1}{1+2\eta\gamma}f - \frac{2\gamma}{1+2\eta\gamma}\right] = \frac{1}{1+2\eta\gamma}f_k + \frac{2\gamma}{1+2\eta\gamma} \quad (25)$$

k is subscript in above equation that represent iteration level.

$$A_k = \frac{1}{1+2\eta\gamma}f_k + \frac{2\gamma}{1+2\eta\gamma} \quad (26)$$

$$B_k = -\left(\frac{\partial h}{\partial F}\right)_k = -\left[\frac{2F}{1+2\eta\gamma} + \frac{M+k}{1+2\eta\gamma}\right]_k = -\frac{2F_k}{1+2\eta\gamma} - \frac{M+K}{1+2\eta\gamma}$$

$$B_k = -\frac{2F_k}{1+2\eta\gamma} - \frac{M+K}{1+2\eta\gamma}$$

$$D_k = h(\eta, F_k, F'_k) - \left(\frac{\partial h}{\partial F}\right)_k F_k - \left(\frac{\partial h}{\partial F'_k}\right)_k F'_k$$

$$D_k = h(\eta, F_k, F'_k) + B_k F_k + A_k F'_k$$

Hence the linear equation for F is given as:

$$F''_{k+1} + A_k F'_{k+1} + B_k F_{k+1} = h(x, F_k, F'_k) + B_k F_k + A_k F'_k \quad (27)$$

Eqs. (18) and (20) are already linear in the variable f and θ , these don't need to be linearized. Rearranging Eq. (20):

$$\theta'' + \left[\frac{2\gamma}{(1+2\eta\gamma)(3R+4)} + \frac{Prf}{(1+2\eta\gamma)(3R+4)} \right] \theta' - \frac{PrnF}{(1+2\eta\gamma)(3R+4)} \theta = 0$$

Let us consider

$$A_k = \frac{2\gamma}{(1+2\eta\gamma)(3R+4)} + \frac{Prf}{(1+2\eta\gamma)(3R+4)} \quad (28)$$

$$B_k = -\frac{PrnF}{(1+2\eta\gamma)(3R+4)}$$

$$D_k = 0$$

Thus

$$\theta'' + A_k \theta' + B_k \theta = D_k$$

Eqs. (4), (7) and (8) are now linear and will be solved as linear second order differential equation iteratively. Thus the system of equations to be solved is as follow:

$$\begin{cases} f'_{k+1} = F_k \\ F''_{k+1} + A_k F'_{k+1} + B_k F_{k+1} = h(x, F_k, F'_k) + B_k F_k + A_k F'_k \\ \theta''_{k+1} + A_k \theta'_{k+1} + B_k \theta_{k+1} = D_k \end{cases} \quad (29)$$

Along with the boundary conditions of Eq. (20):

$$\begin{cases} \eta = 0, & f(0) = s, F(0) = -1 + \lambda_1 F'(0) + \lambda_2 F''(0), \\ & \theta(0) = 1 + \beta \theta'(0) \\ \eta = \infty, & \eta \rightarrow \infty : F(\infty) = 0, \theta(\infty) = 0 \end{cases} \quad (30)$$

Following the linearization of the equations, the Galerkin finite difference method was incorporated into the Finite Element Method (FEM) for solving the three linear equations in (29). The methodology involved several steps:

- Discretization of the domain: The domain was discretized into finite elements, with each element represented by selected basis functions, in accordance with standard FEM procedures.
- Assembly of the global system of equations: Local contributions from all elements were aggregated to form the global system of equations, ensuring compliance with the prescribed boundary conditions.
- Application of the Galerkin finite difference method: Within each finite element, the Galerkin finite difference method was applied to approximate the solution of the differential equations governing fluid flow and heat transfer. This method employs weighted residual techniques to minimize the error between the approximate and exact solutions.
- Solution of the linear equations: The resulting linear equations were numerically solved using MATLAB or a similar computational tool, which facilitated

efficient matrix manipulations and equation solving.

- Visualization of results: The numerical solutions obtained through this combined approach were visualized to analyze the complex interplay among magnetohydrodynamic effects, second-order slip dynamics, and radiative heat transfer.

By integrating the Galerkin finite difference method with the FEM, our study aimed to achieve precise and robust numerical solutions, contributing to a comprehensive understanding of fluid flow and heat transfer phenomena around the stretching cylinder.

Finite element method at first will be used for the second equation of (29). Coefficient of this equation are evaluated by numerical differentiation which are given by Eqs. (32), (33) and (34). Second equation of (13) is given by:

$$F''_{k+1} + A_k F'_{k+1} + B_k F_{k+1} = D_k \quad (31)$$

Numerical differentiation of coefficients are given by:

$$\begin{aligned} h(\eta, F_k, F'_k) &= \frac{1}{1+2\eta_i\beta} (F_i)_k^2 \\ &\quad - \frac{1}{1+2\eta_i\beta} (f_i)_k \left(\frac{F_{i+1} - F_{i-1}}{2\Delta\eta} \right)_k \\ &\quad - \frac{2\beta}{1+2\eta_i\beta} \left(\frac{F_{i+1} - F_{i-1}}{2\Delta\eta} \right)_k \\ &\quad + \frac{M+k}{1+2\eta_i\beta} (F_i)_k \\ &\quad - \frac{Gr}{1+2\eta_i\beta} (\theta_i)_k \\ A_k &= \frac{1}{1+2\eta_i\gamma} (f_i)_k + \frac{2\gamma}{1+2\eta_i\gamma} \end{aligned} \quad (32)$$

With $i = 2$ to N , the subscript n represent the previous iteration and i is for interior nodes only. We will require an initial guess to start the iterations process.

$$B_k = -\frac{2(F_i)_k}{1+2\eta_i\gamma} - \frac{M+k}{1+2\eta_i\gamma} \quad (33)$$

$$\begin{aligned} h(\eta, F_n, F'_n) &= -f_n \frac{(F_{i+1} - F_{i-1})_n}{2\Delta\eta} \\ &\quad - \frac{\eta\alpha_1 (F_{i+1} - F_{i-1})_n}{2 \cdot 2\Delta\eta} \\ &\quad - (\alpha_1 - M)(F_i)_n + (F_i)_n^2 - G_r \theta \\ &\quad - G_c \phi \end{aligned} \quad (34)$$

$$D_k = h(\eta, F_k, F'_k) + B_k (F_i)_k + A_k \left(\frac{F_{i+1} - F_{i-1}}{2\Delta\eta} \right)_k$$

Multiplying Eq. (12) to a weight function $w(\eta)$ and integrating over the domain $[a, b]$.

$$\begin{aligned} \int_a^b \left(\frac{d^2 F_{k+1}}{d\eta^2} + A_k \frac{dF_{k+1}}{d\eta} + B_k F_{k+1} \right) w(\eta) d\eta \\ = \int_a^b D_k w(\eta) d\eta \end{aligned} \quad (35)$$

$$\int_a^b \frac{d^2 F_{k+1}}{d\eta^2} w(\eta) d\eta + \int_a^b A_k \frac{dF_{k+1}}{d\eta} w(\eta) d\eta + \int_a^b B_k F_{k+1} w(\eta) d\eta = \int_a^b D_k w(\eta) d\eta \quad (36)$$

Integrating the left hand side by parts:

$$\left[\frac{dF_{k+1}}{d\eta} w \right]_a^b - \int_a^b \frac{dF_{k+1}}{d\eta} \frac{dw}{d\eta} d\eta + \int_a^b A_k \frac{dF_{k+1}}{d\eta} w(\eta) d\eta + \int_a^b B_k F_{k+1} w(x) d\eta = \int_a^b D_k w(x) d\eta \quad (37)$$

$$\left[\frac{dF_{k+1}(b)}{d\eta} w(b) - \frac{dF_{k+1}(a)}{d\eta} w(a) \right] - \int_a^b \frac{dF_{k+1}}{dx} \frac{dw}{dx} dx + \int_a^b A_k \frac{dF_{k+1}}{dx} w(\eta) d\eta + \int_a^b B_k F_{k+1} w(\eta) d\eta = \int_a^b D_k w(\eta) d\eta \quad (38)$$

Weight function $w(\eta)$ is chosen in such a way that it has zero value in case of Dirichlet boundary conditions. Dirichlet boundary condition is mentioned at last node of the domain that is $w(b) = 0$. Therefore, above equation will become:

$$-\frac{dF_{k+1}(a)}{d\eta} w(a) - \int_a^b \frac{dF_{k+1}}{d\eta} \frac{dw}{d\eta} d\eta + \int_a^b A_k \frac{dF_{k+1}}{d\eta} w(\eta) d\eta + \int_a^b B_k F_{k+1} w(\eta) d\eta = \int_a^b D_k w(\eta) d\eta \quad (39)$$

Boundary condition at first node is written as follow:

$$F(0) = -1 + \lambda_1 F'(0) + \lambda_2 F''(0) \quad (40)$$

Using forward approximation as follow:

$$F_0 = -1 + \lambda_1 \frac{(F_1 - F_0)}{\Delta\eta} + \lambda_2 \frac{(F_2 - 2F_1 + F_0)}{\Delta\eta^2} \left[1 + \frac{\lambda_1}{\Delta\eta} - \frac{\lambda_2}{\Delta\eta^2} \right] F_0 + \left[-\frac{\lambda_1}{\Delta\eta} + \frac{2\lambda_2}{\Delta\eta^2} \right] F_1 - \frac{\lambda_2}{\Delta\eta^2} F_2 = -1 \quad (41)$$

First equation in the whole matrix is replaced by above equation.

$$-\int_a^b \frac{dF_{k+1}}{d\eta} \frac{dw}{d\eta} d\eta + \int_a^b A_k \frac{dF_{k+1}}{d\eta} w(\eta) d\eta + \int_a^b B_k F_{k+1} w(\eta) d\eta = \int_a^b D_k w(\eta) d\eta \quad (42)$$

Eq. (42) is the weak formulation of (41). Let the solution of (20) is of the following form:

$$F_{k+1} = \sum_{i=1}^{Ne} \phi_i(F_{k+1})_i$$

ϕ_i are the basis function and Ne are the total number of nodes in an element.

Galerkin Finite element method requires that basis function for weight function must also be same as defined above.

After selecting appropriate weight functions, the domain was discretized into finite elements. These elements were underpinned by chosen basis functions, crucial for accurate approximations of the unknown solution within each element. The global system of equations was assembled through the aggregation of local contributions from all elements, while adhering to Dirichlet boundary conditions by ensuring zero values in the chosen weight functions at the boundary nodes. The ensuing linear system was effectively solved utilizing the versatile MATLAB software, which facilitated matrix manipulations, equation solving, and result visualization. The subsequent stages encompassed post-processing and result visualization, shedding light on the system's intricate behaviour. This comprehensive methodology underscores the synergy of Finite Element Method principles, encompassing basis functions and the global stiffness matrix, coupled with MATLAB's computational power to unravel complex real-world scenarios, leading to robust simulations and profound insights.

4. RESULT AND DISCUSSION

To ascertain the precision of our employed numerical technique, we conduct a direct comparison between our computed values of $f''(0)$ and those documented by Fang et al. [17] and Mishra and Singh [21], as illustrated in Table 1 for the specific instance of the problem under investigation.

Remarkably, the outcomes yield corresponding graph plots and results, demonstrating a strong alignment and bolstering the dependability of our approach, even while omitting the radiation parameter R , the magnetic parameter M , and the permeability parameter k . This comparison, which showcases a notable agreement among the diverse flow parameters, underscores the confidence we hold in the accuracy and trustworthiness of our numerical results.

Eqs. (10) and (11), together with the specified boundary conditions (12), are numerically solved. Notably, the system of equations yields dual solutions, referred to as the first and second solutions. The key quantities of interest encompass $f''(0)$, which characterizes skin friction or the drag experienced by the surface, and $-\theta'(0)$, representing the surface's heat transfer rate from fluid. Additionally, $f'(0)$ denotes the fluid

velocity at the surface, while $\theta(0)$ signifies the fluid temperature at the surface. Further, the fluid velocity and temperature distributions are captured by $f(\eta)$ and $\theta(\eta)$, respectively. This section delves into a comprehensive exploration of the physical parameters brought forth by these solutions.

From Figures 2 and 3, a clear pattern emerges: In the first solution, the fluid velocity and temperature exhibit a decline as 's' increases. Notably, as 's' increases, the velocity boundary layer thickness also decreases a phenomenon consistent with the anticipated behavior of boundary layers thinning out due

to increased suction. Transitioning to the second solution, Figures 2 and 3 continue to elucidate the relationship: as 's' grows, fluid velocity and temperature decrease. Strikingly, the trends observed for the second solution mirror those of the first, yet with a notable distinction. The second solution's velocity and thermal boundary layer thicknesses surpass those of the first, and intriguingly, the velocity boundary layer thickness does not diminish as 's' increases. This revelation paints a comprehensive picture of how variations in 's' intricately affect fluid dynamics and thermal behavior in both solutions.

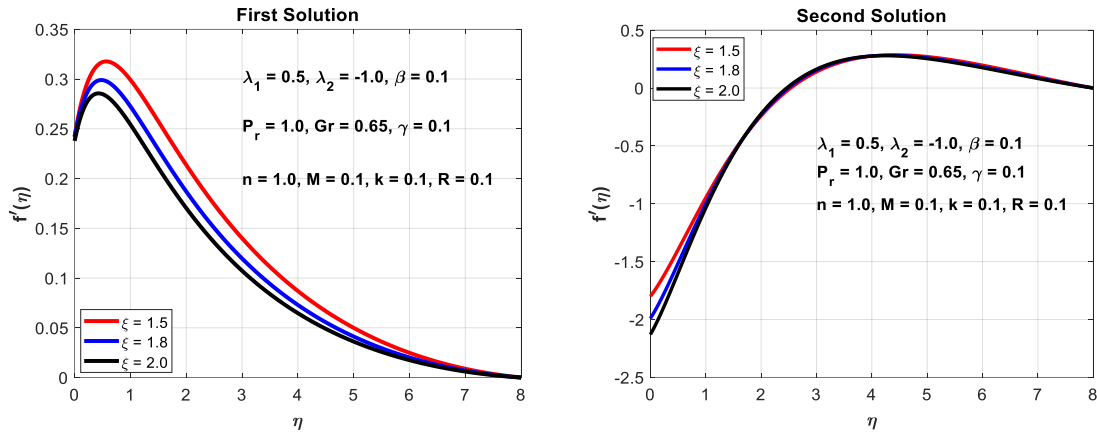


Figure 2. Variation of velocity $f'(\eta)$ with η with several values of ξ

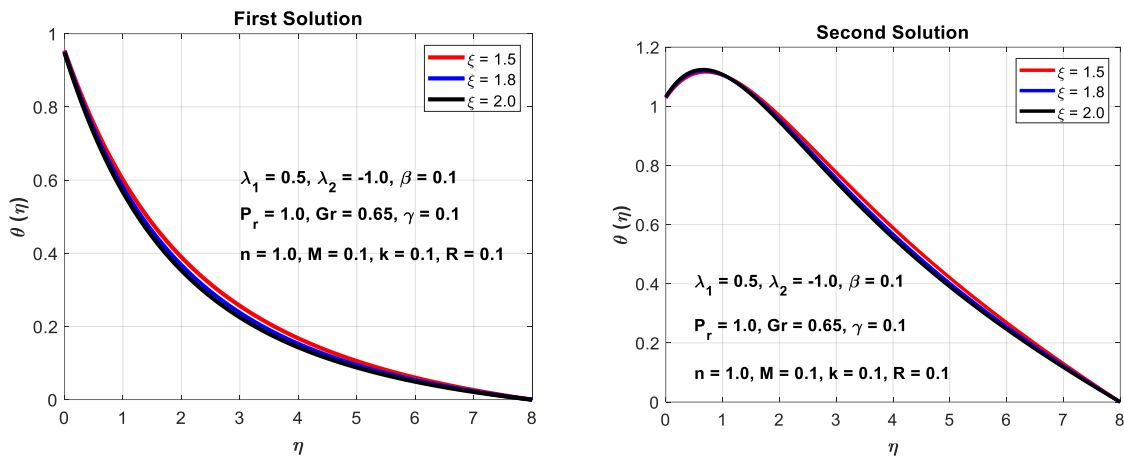


Figure 3. Variation of temperature $\theta(\eta)$ with η with several values of ξ

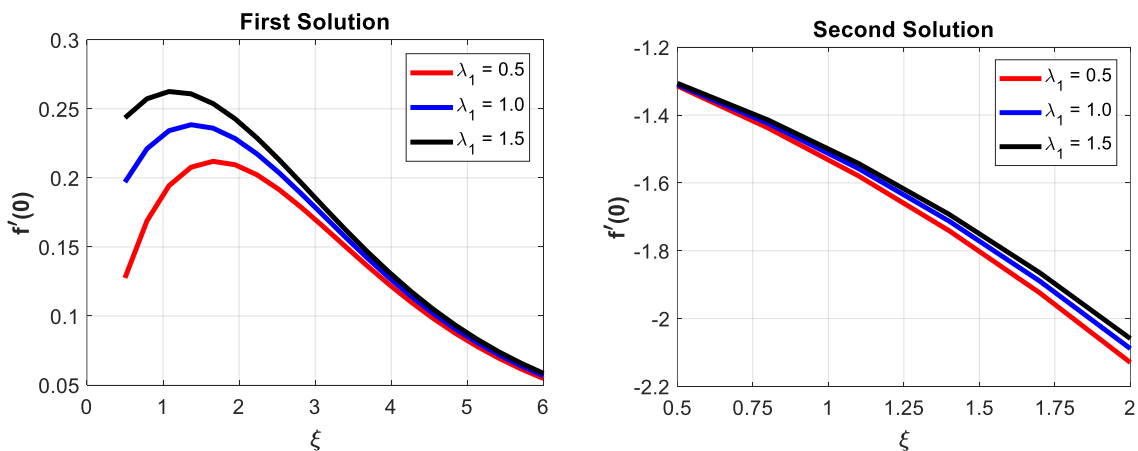


Figure 4. Variation of velocity $f'(\eta)$ with ξ with several values of λ_1

Analyzing Figure 4, a compelling trend becomes apparent within the first solution: an increase in the value of the first-order slip parameter (λ_1) corresponds to a rise in $f(0)$, signifying a higher fluid velocity at the surface. This behavior aligns with the concept of slip flow, where an increase in slip induces a higher flow velocity in the vicinity of the surface. The second solution follows a similar trend, where an elevated (λ_1) value leads to an increment in $f(0)$. This outcome aligns with the notion that a larger slip parameter enhances the fluid flow near the surface. Shifting focus to Figure 5, a deeper narrative unfolds. In the first solution, augmenting the slip parameter (λ_1) brings about a reduction in $f''(0)$, indicating a decrease in the rate of change of fluid velocity gradient at the surface. This observation can be attributed to the phenomenon that slip effects tend to smoothen velocity gradients near the surface. This behavior resonates within the second solution as well, where an increase in (λ_1) leads to a decline in $f''(0)$.

In Figure 6, an intriguing interplay unfolds within the first solution. As the value of (λ_1) increases, there is a slight decrease in $\theta(0)$, the fluid temperature at the surface. While this decrease is minor, its significance underscores the influence of (λ_1) on heat transfer. Alternatively, with the elevation of ξ , a more pronounced decrease in $\theta(0)$ occurs a behavior anticipated due to augmented suction promoting cooler surface temperatures. Meanwhile, in the second solution, a different dynamic arises. With increasing (λ_1), $\theta(0)$ experiences an increase, signifying enhanced fluid temperature at the surface. However, as ξ rises for a fixed (λ_1), the surface temperature, $\theta(0)$, decreases an outcome aligning with the cooling effect of increased suction. Shifting to Figure

7, a nuanced observation emerges for the first solution. With the augmentation of (λ_1), the parameter $\theta'(0)$, which represents the rate of heat transfer from the surface to the fluid, experiences a minor increase. For a consistent (λ_1) value, this increase remains subtle. Contrastingly, within the second solution, elevating (λ_1) leads to a decrease in $\theta'(0)$, signifying a reduction in heat transfer rate due to increased slip effects. Similarly, for a fixed (λ_1), the interaction of increased ξ yields an elevation in $\theta'(0)$, suggesting enhanced heat transfer due to augmented surface shear.

Figures 8(a) and 9(a) elucidate the intricate dynamics of the first solution. Notably, as the parameter (λ_1) increases, the fluid velocity experiences a corresponding rise, signifying an intensified flow near the surface. Simultaneously, a minor decline in fluid temperature becomes apparent. This modest temperature reduction emphasizes the nuanced interplay between increased velocity and the resulting heat transfer. In Figure 8(b), a distinctive observation arises within the second solution. The fluid velocity profiles for different (λ_1) values intersect, indicating the complexity of the relationship between (λ_1) and velocity. It becomes evident that the impact of (λ_1) on fluid velocity is not straightforward, warranting further investigation. In contrast, fluid temperature responds more predictably to (λ_1). As seen in Figure 9(b), the second solution showcases an increase in fluid temperature with higher (λ_1) values. This outcome resonates with the understanding that increased slip effects, linked to elevated (λ_1) lead to less efficient heat dissipation, resulting in elevated fluid temperatures.

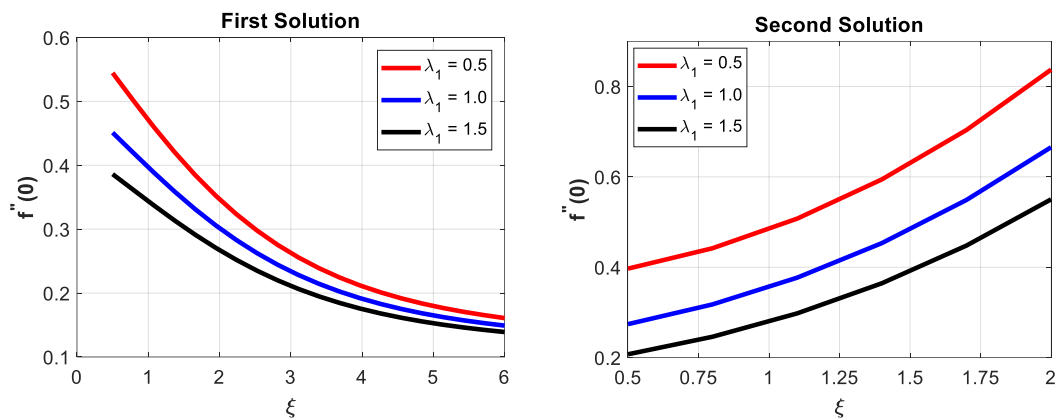


Figure 5. Variation of velocity $f''(0)$ with ξ with several values of λ_1

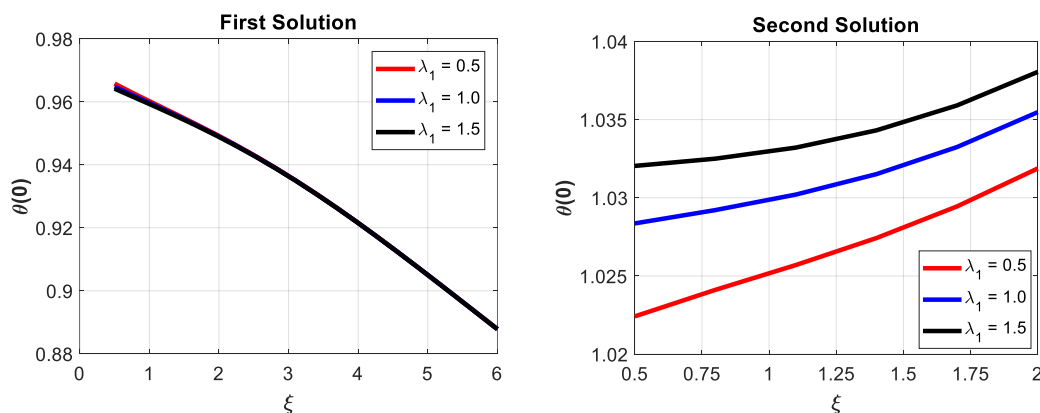


Figure 6. Variation of temperature $\theta(0)$ with ξ with several values of λ_1

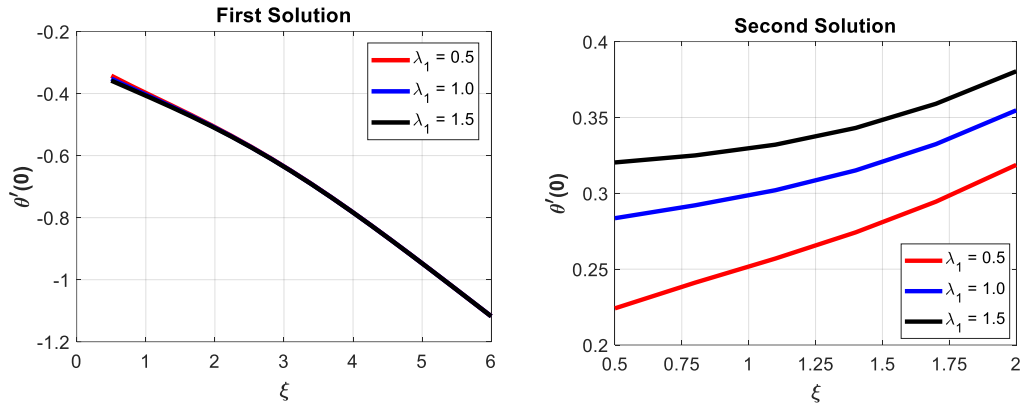


Figure 7. Variation of temperature $\theta'(0)$ with ξ with several values of λ_1

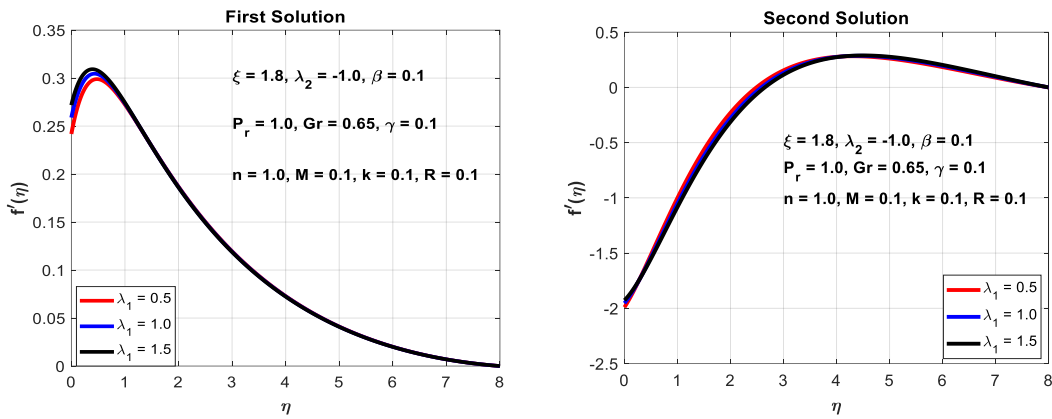


Figure 8. Variation of velocity $f'(\eta)$ with η with several values of λ_1

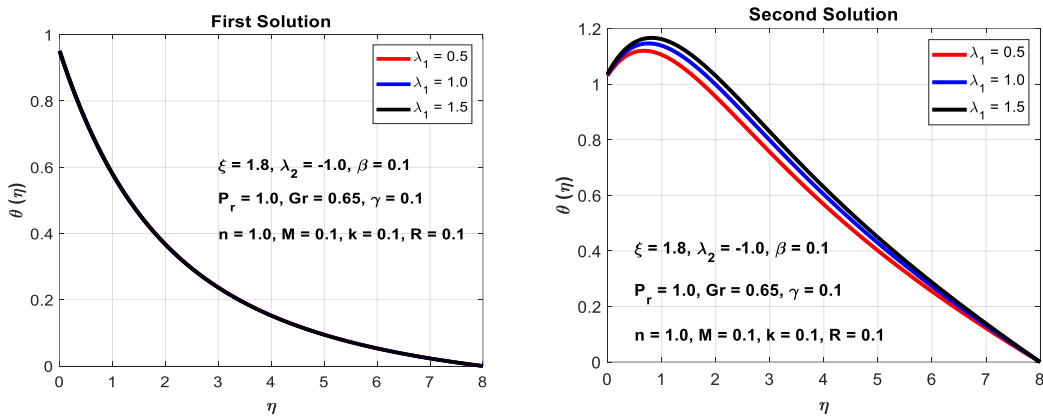


Figure 9. Variation of temperature $\theta'(\eta)$ with η with several values of λ_1

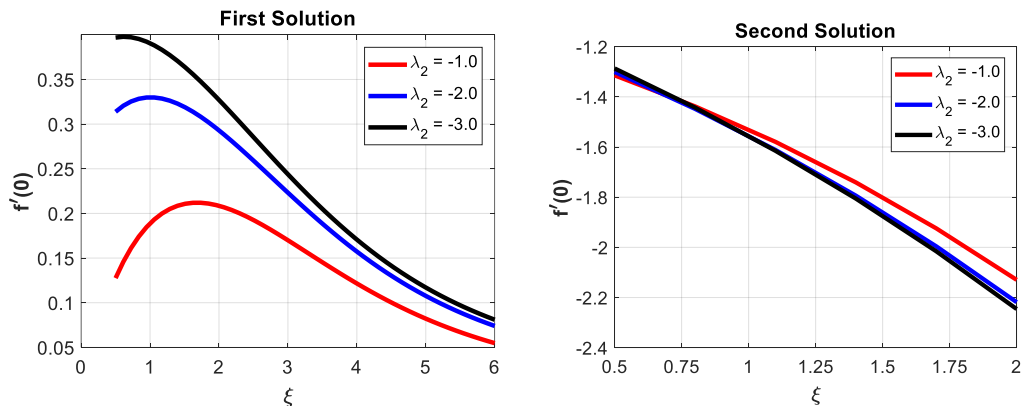


Figure 10. Variation of velocity $f'(0)$ with ξ with several values of λ_2

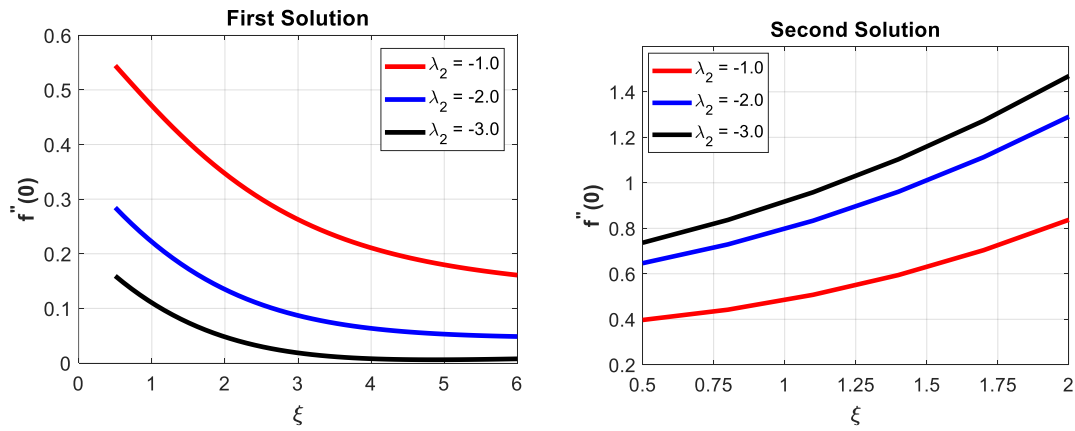


Figure 11. Variation of velocity $f''(0)$ with ξ with several values of λ_2

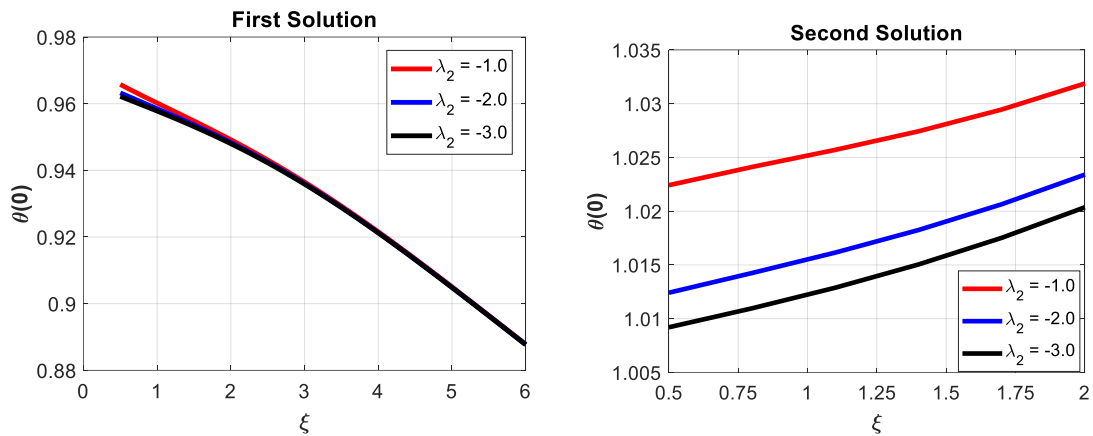


Figure 12. Variation of temperature $\theta(0)$ with ξ with several values of λ_2

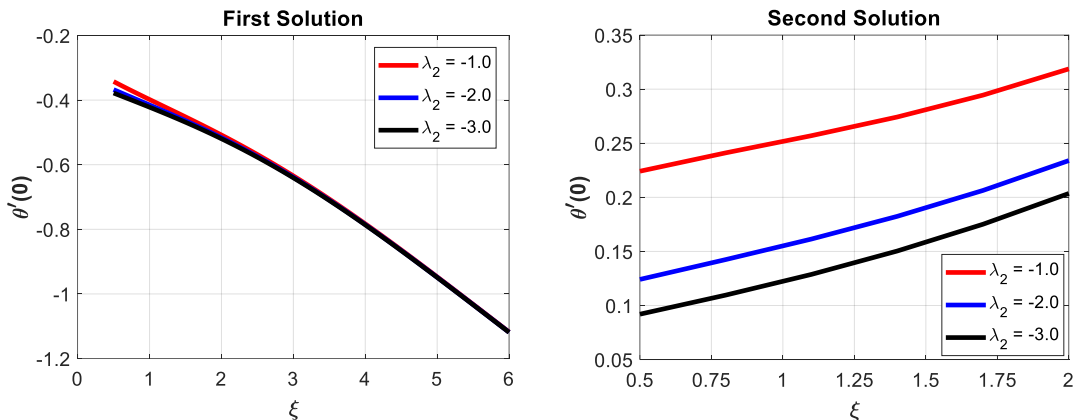


Figure 13. Variation of temperature $\theta'(0)$ with ξ with several values of λ_2

Examining Figure 10, a noteworthy pattern emerges a reduction in the second order slip parameter (λ_2) results in an increase in $f''(0)$ for first solution and decrease in second solution. This behavior can be interpreted in terms of reduced slip effects, where a smaller (λ_2) leads to enhanced fluid adhesion to the surface, thereby amplifying the flow velocity near the surface. In Figure 11, a contrasting trend is evident. For the first solution, as (λ_2) decreases, there's a reduction in $f''(0)$, reflecting a less steep change in fluid velocity gradient near the surface. This phenomenon can be attributed to reduced slip effects, which tend to smoothen velocity gradients. Interestingly, the second solution showcases an increase in $f''(0)$ with reduced (λ_2), suggesting a complex interplay between slip effects and velocity profiles.

Reviewing Figure 12, an intriguing insight emerges

regarding the role of parameter (λ_2) within the first solution. Remarkably, its impact seems to be minimal, suggesting that changes in (λ_2) have negligible effects on the behavior of the first solution. In contrast, the second solution paints a different picture. As (λ_2) decreases, a distinct trend arises—there's a reduction in $\theta(0)$, the fluid temperature at the surface. This phenomenon can be attributed to the intricate interplay between slip effects, surface adhesion, and the thermal dynamics governing the second solution. Shifting focus to Figure 13, a parallel narrative unfolds. For the first solution, the influence of (λ_2) on $-\theta'(0)$, which characterizes the rate of change of temperature gradient at the surface, seems to be marginal. However, within the context of the second solution, a prominent shift becomes apparent. Decreasing (λ_2) correlates with a noteworthy increase in $-\theta'(0)$.

In Figure 14(a) and 15(a), a discernible pattern unfolds as the parameter (λ_2) decreases, the fluid velocity experiences an increase. This phenomenon can be attributed to reduced slip effects, allowing for a stronger fluid adhesion to the surface and thus a swifter flow. Interestingly, the variation in fluid temperature appears negligible, suggesting that (λ_2) might not significantly influence temperature dynamics within this context. Moving to Figure 14(b), a distinct observation emerges—there's no evident trend. This lack of clear behavior underscores the complexity of the relationship between (λ_2) and the depicted parameter, potentially indicating the nuanced nature of the system's response. Shifting focus to Figure 15(b), a pronounced trend is evident: a decrease in (λ_2) corresponds to a reduction in fluid temperature. This observation resonates with the concept that decreased slip effects lead to improved

thermal contact between the fluid and the surface, thereby lowering the fluid temperature. These findings collectively unravel the multifaceted interplay between slip effects, fluid velocity, and temperature changes with varying (λ_2).

Figures 16-19 provide a comprehensive insight into the behavior of the first solution. As the parameter δ increases, a consistent pattern emerges across various variables. Specifically, $f'(0)$, $f''(0)$, $\theta(0)$, and all exhibit a decrease. This observation is attributed to the influence of δ on slip effects: an elevated δ value corresponds to reduced fluid adhesion to the surface. Consequently, fluid velocity, its gradients, and surface temperature all experience a decline. On the other hand, within the context of the second solution, an opposing trend takes center stage. An increase in δ coincides with $f(0)$ augmentation, while $f''(0)$, $\theta(0)$, and $-\theta'(0)$ all decrease.

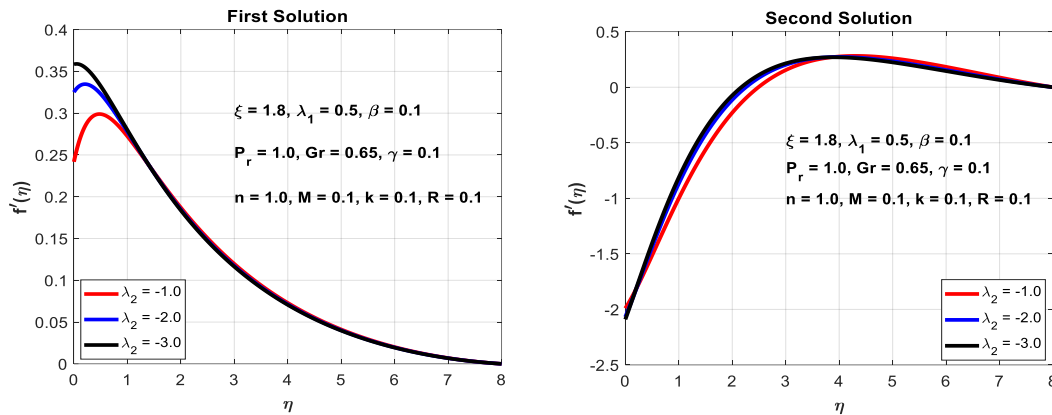


Figure 14. Variation of velocity $f'(\eta)$ with η with several values of λ_2

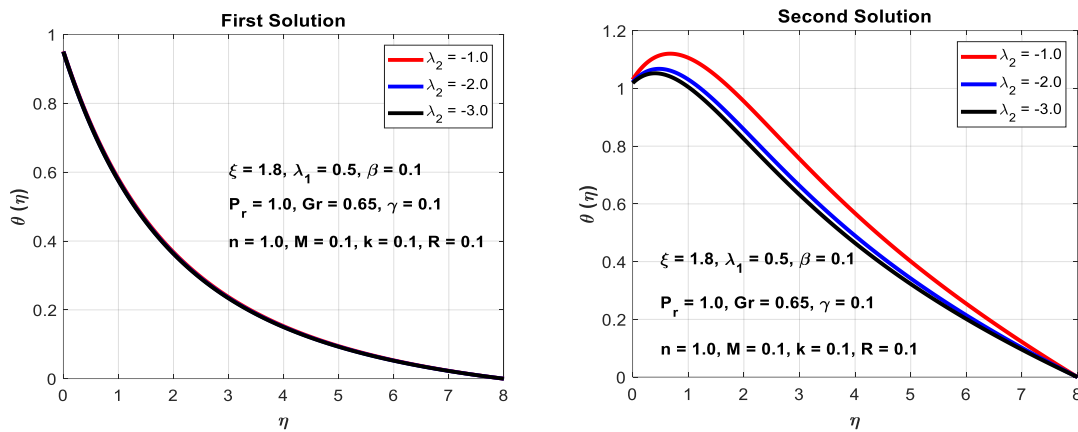


Figure 15. Variation of temperature $\theta(\eta)$ with η with several values of λ_2

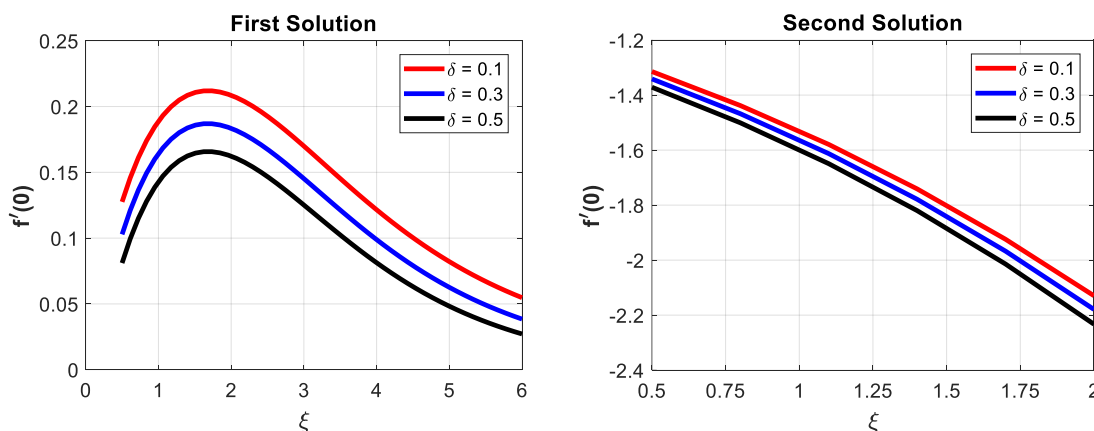


Figure 16. Variation of velocity $f'(0)$ with ξ with several values of δ

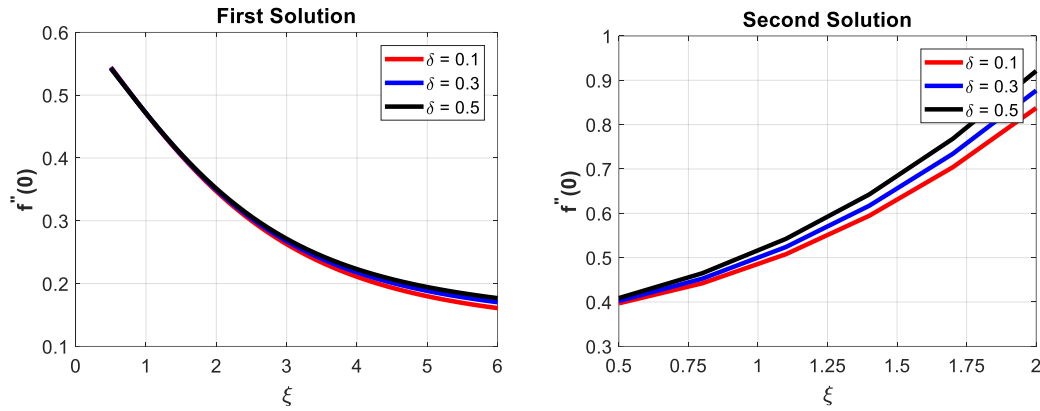


Figure 17. Variation of velocity $f''(0)$ with ξ with several values of δ

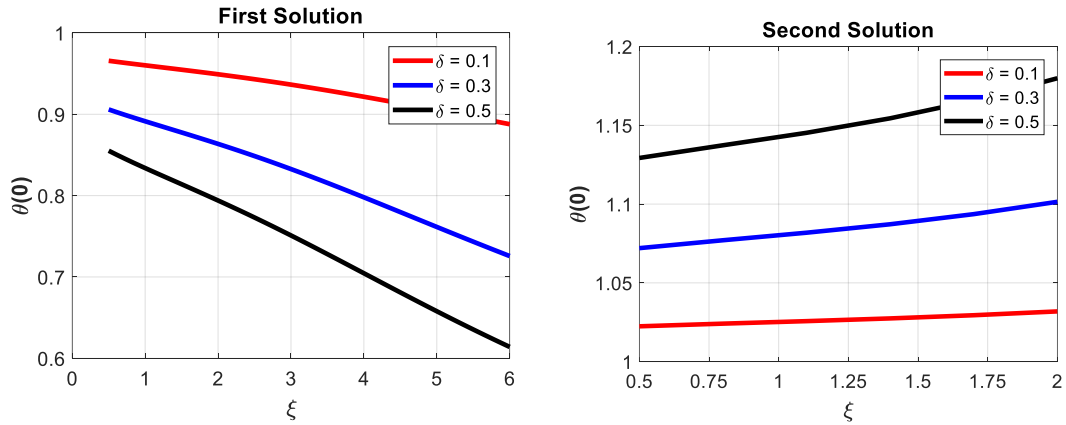


Figure 18. Variation of temperature $\theta(0)$ with ξ with several values of δ

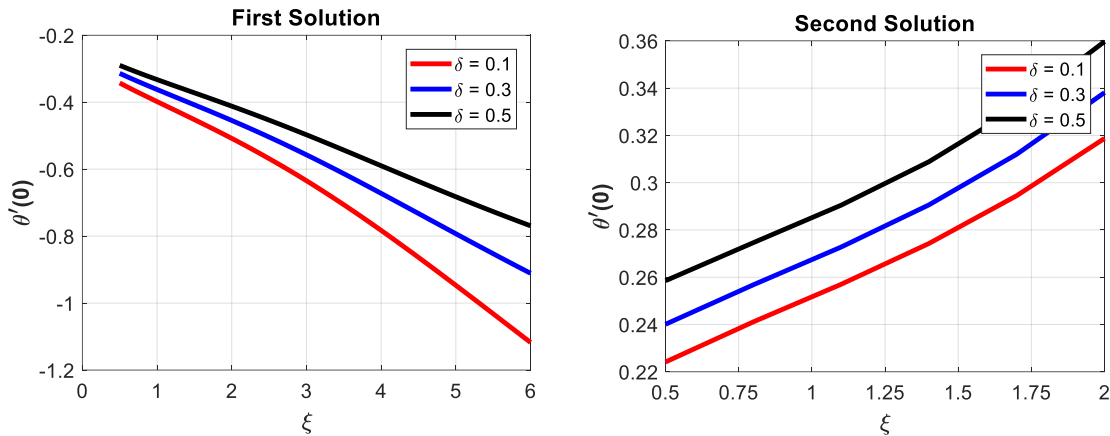


Figure 19. Variation of temperature $\theta'(0)$ with ξ with several values of δ

Figures 20(a) and 21(a) offer a revealing insight into the system's dynamics. As δ experiences an increase, both fluid velocity and temperature demonstrate a noteworthy decrease. This observation can be attributed to the augmented slip effects resulting from higher δ . These slip effects tend to hinder fluid motion near the surface, leading to reduced velocity and subsequently, cooler temperatures. Contrasting this, Figure 20(b) reveals a lack of clear trend in fluid velocity concerning the thermal slip parameter δ . This nuanced response underscores the intricate interplay between δ and fluid velocity, indicating that other factors might be at play. However, the fluid temperature's behavior is more pronounced. As depicted in Figure 21(b), a consistent pattern emerges—fluid temperature diminishes as δ increases. This outcome aligns with the notion that increased slip effects, linked to

higher δ , result in improved thermal insulation between the fluid and the surface, leading to a cooling effect.

Examining Figures 22 reveals the velocity profile and provides intriguing insights. As the Grashof number (Gr) experiences an increment, $f'(\eta)$ demonstrates contrasting behaviors within the two solutions. In the first solution, there's an augmentation in $f'(\eta)$, indicating an intensified fluid motion near the surface due to higher Gr values. Conversely, the second solution witnesses a reduction in $f'(\eta)$, signifying a damping effect on fluid velocity with elevated Gr . This behavior is linked to the interplay between buoyancy-driven forces and slip effects, which govern fluid motion in the presence of gravity. Moreover, focusing on temperature profiles in Figure 23, a consistent trend emerges with increasing Gr for both solutions. In both the first and second

solutions, an increase in Gr corresponds to a decrease in temperature profiles. This cooling effect can be attributed to the enhanced convective heat transfer brought about by larger Gr values.

The transverse curvature parameter captures a geometric characteristic of a cylinder. Figures 23(a) and 24(a) bring to light a notable phenomenon as the parameter γ experiences an increase, both fluid velocity and temperature exhibit a rise. This observation can be attributed to the impact of γ on the cylinder's transverse curvature. An elevated γ value signifies a more slender cylinder, which in turn enhances fluid flow and heat transfer near the surface. Intriguingly, the increase in γ

also leads to an augmentation in the velocity boundary layer thickness. This expansion is linked to the altered fluid dynamics resulting from the changing cylinder shape. Turning our attention to Figure 23(b), a distinct behavior emerges fluid velocity does not follow a clear trend as γ increases. This complex response might stem from the intricate interplay between fluid flow dynamics and the geometry of the cylinder. Finally, in Figure 24(b), a coherent pattern arises an increase in γ corresponds to a rise in fluid temperature. This temperature elevation can be attributed to enhanced heat transfer due to the altered fluid flow patterns near the surface of the cylinder with changing curvature.

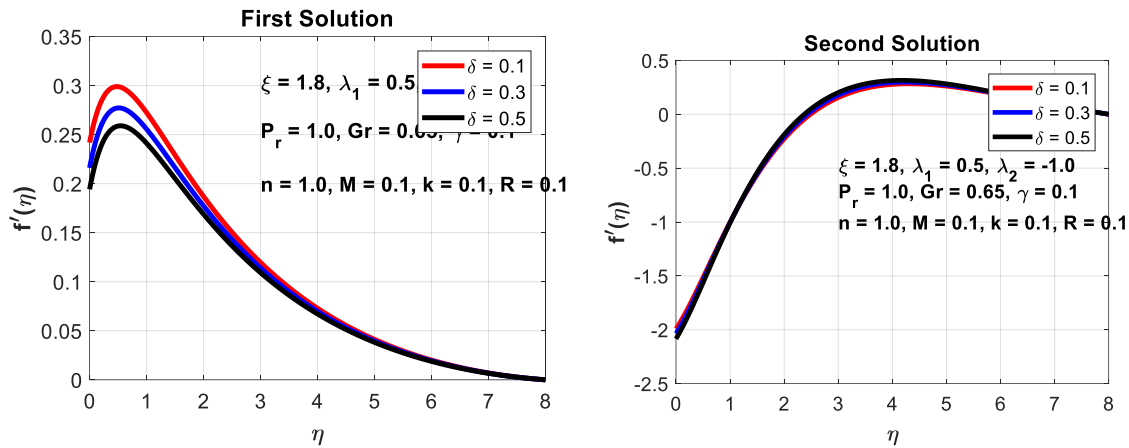


Figure 20. Variation of velocity $f'(\eta)$ with η with several values of δ

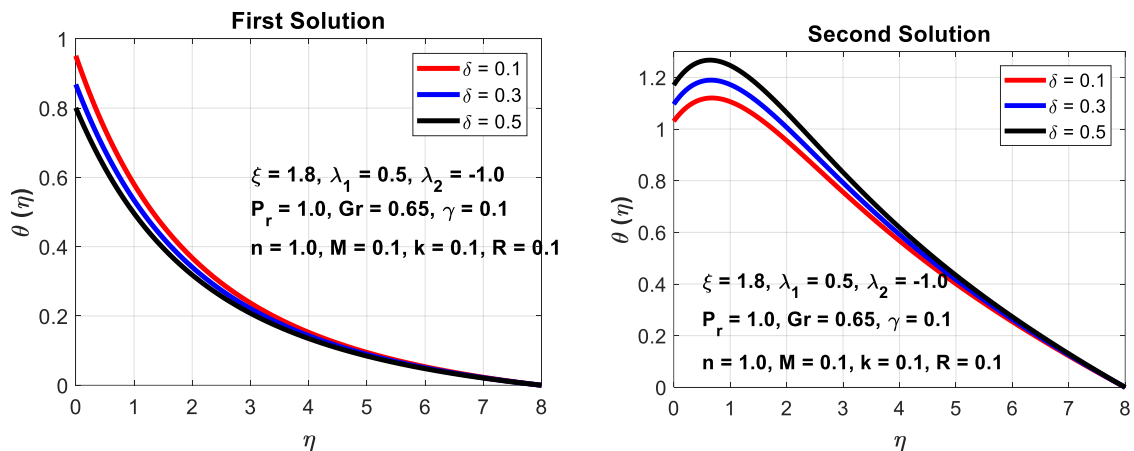


Figure 21. Variation of temperature $\theta(\eta)$ with η with several values of δ

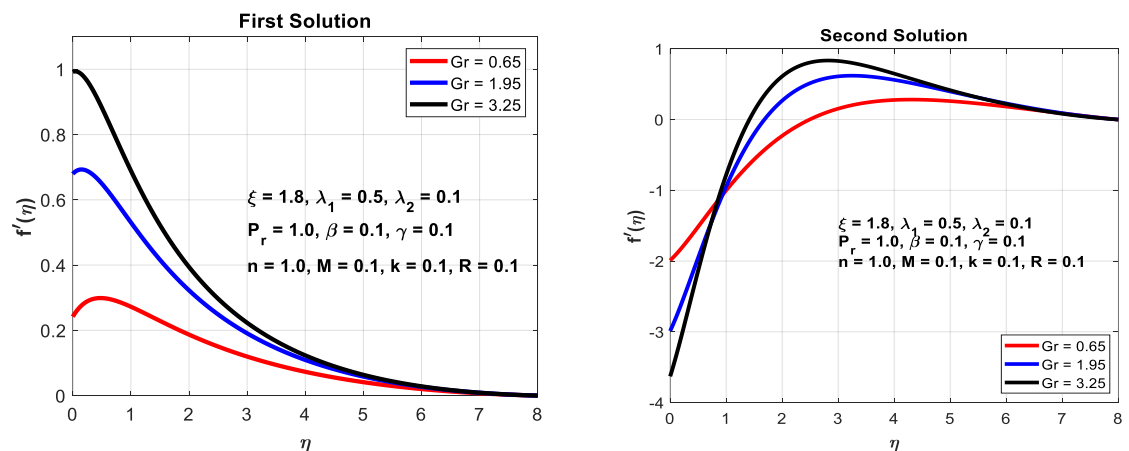


Figure 22. Variation of velocity $f'(\eta)$ with η with several values of Gr

Figures 25(a) and 26(a) unveil a compelling insight: as the Prandtl number (Pr) increases, both fluid velocity and temperature experience a decline. This observation can be attributed to the inherent characteristics of the fluid and its thermal behavior. A higher Prandtl number indicates a fluid that is less conductive thermally, which in turn influences its capacity to transfer heat efficiently. Consequently, an elevated Prandtl number leads to reduced fluid velocities and lower temperature levels. Furthermore, the effects of Prandtl number are evident in boundary layer dynamics. As Pr increases, both the velocity and thermal boundary layer thickness decrease.

This behavior can be explained by the altered balance between fluid momentum and heat transfer near the surface, influenced by the Prandtl number. In contrast, Figure 25(b) demonstrates a lack of a clear trend in fluid velocity changes with respect to increasing Pr. This complex response reflects the intricate interplay between fluid properties and their interaction with the Prandtl number. Finally, Figure 26(b) portrays a consistent pattern: as Pr increases, fluid temperature decreases. This behavior can be linked to the reduced heat conductivity of fluids with higher Prandtl numbers, which results in less efficient heat transfer and subsequently, lower temperatures.

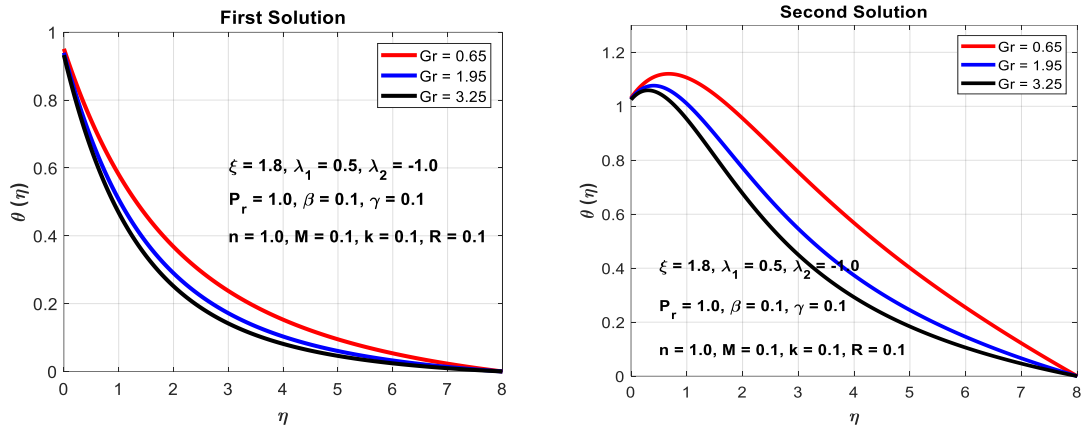


Figure 23. Variation of temperature $\theta(\eta)$ with η with several values of Gr

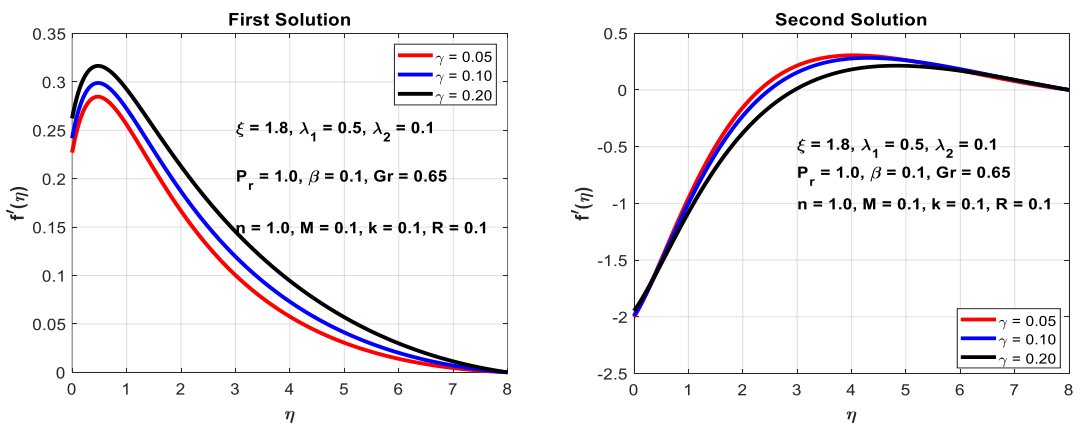


Figure 24. Variation of velocity $f'(\eta)$ with η with several values of γ

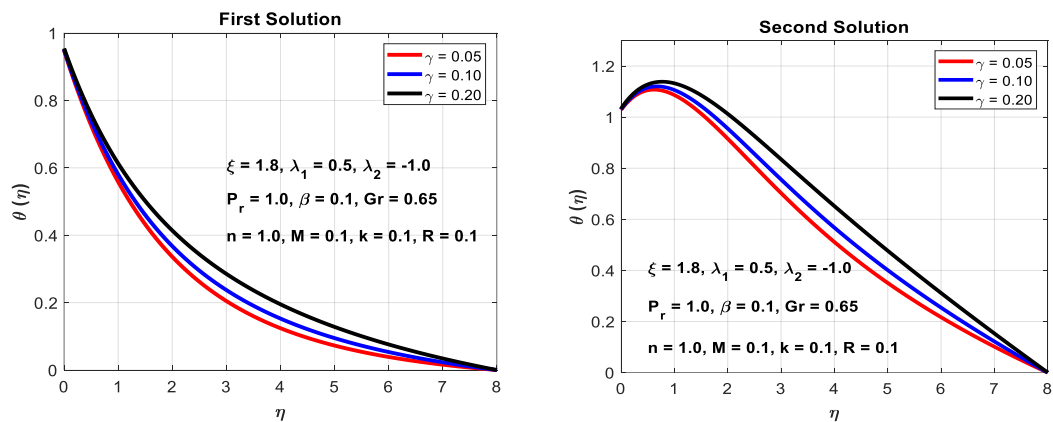


Figure 25. Variation of temperature $\theta(\eta)$ with η with several values of γ

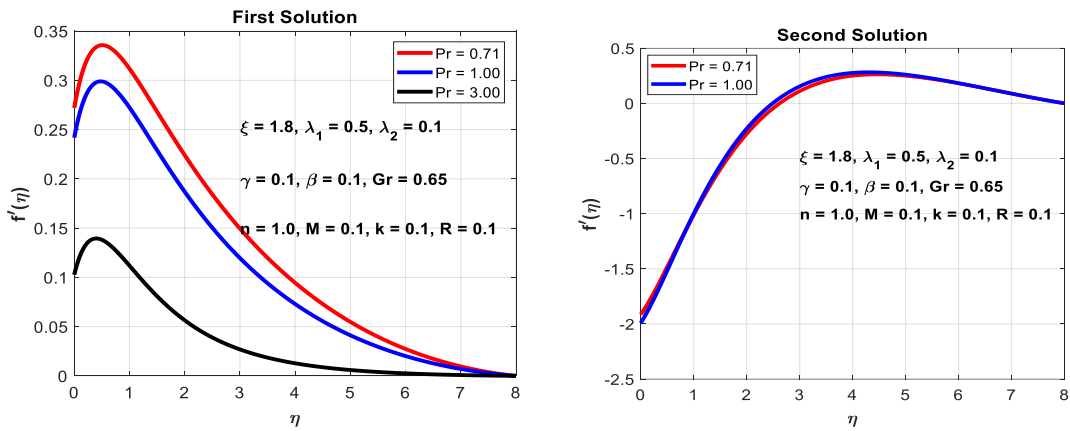


Figure 26. Variation of velocity $f'(\eta)$ with η with several values of Pr

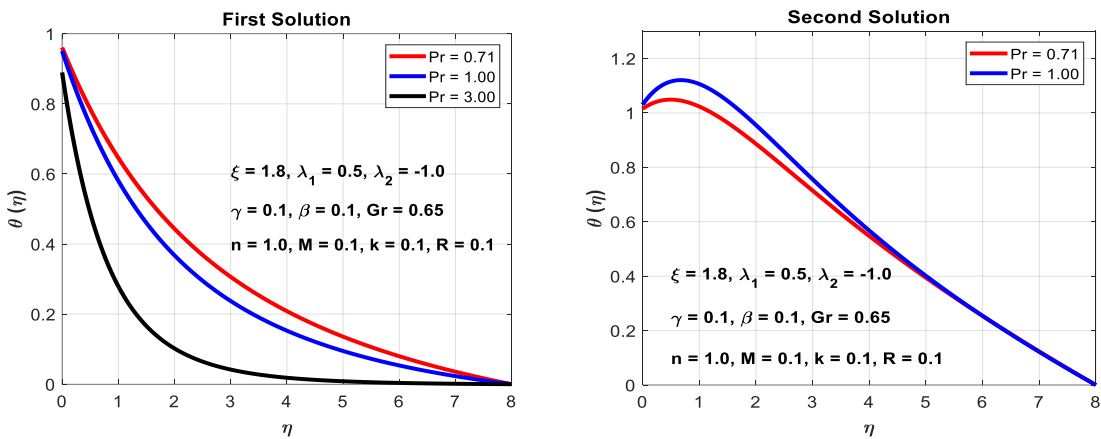


Figure 27. Variation of temperature $\theta(\eta)$ with η with several values of Pr

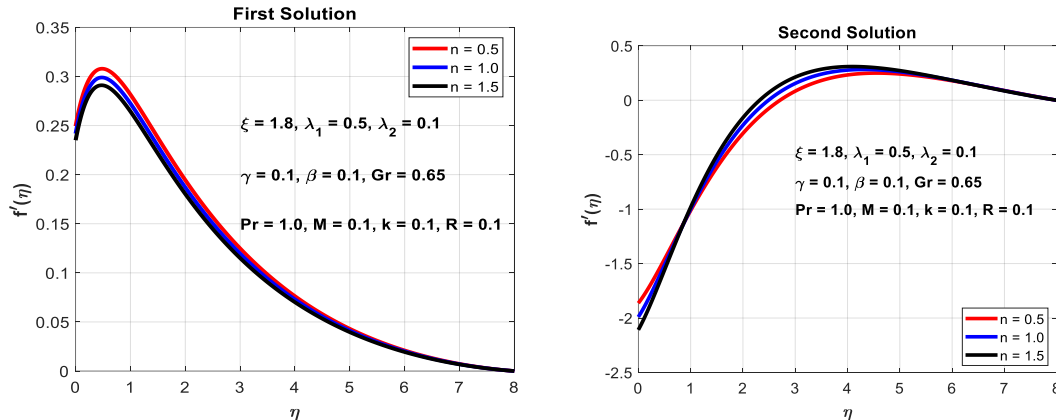


Figure 28. Variation of velocity $f'(\eta)$ with η with several values of n

Figure 27 provides valuable insights into the velocity profile as it fluctuates across different values of the parameter 'n'. Within the context of the first solution, a discernible trend unfolds. The velocity profile diminishes as the temperature exponent 'n' increases. This behavior can be attributed to the intricate interplay between temperature and fluid dynamics. Higher values of 'n' likely lead to intensified thermal effects, impacting fluid motion and dampening the velocity near the surface. Conversely, an intriguing reversal is observed within the second solution. Increasing 'n' corresponds to an augmentation of the velocity profile. Whereas in Figure 28, a depiction of temperature distribution profiles across varying 'n' values is presented. Within the first solution, a clear observation emerges: as the temperature exponent 'n' rises, the temperature profile experiences a decline. This trend aligns

with the notion that elevated 'n' values lead to intensified thermal effects, causing a cooling effect near the surface. On the other hand, the second solution showcases an opposing behavior. Increasing 'n' leads to an elevation in the temperature profile.

Figure 29(a) illustrates the correlation between the magnetic parameter (M) and fluid velocity in the first solution. It is evident that an increase in the value of M leads to a subsequent decrease in fluid velocity. This behaviour can be attributed to the influence of a magnetic field, which imposes a Lorentz force that counteracts fluid motion. Consequently, the observed reduction in fluid velocity as M increases aligns seamlessly with our understanding of how magnetic fields shape fluid dynamics. In contrast, Figure 29(b) sheds light on the impact of M on fluid velocity within the second solution.

Intriguingly, a rise in M results in a reduction of fluid velocity.

Turning to Figure 30(a), we scrutinize the consequences of the magnetic parameter (M) on fluid temperature distribution. Interestingly, the graph unveils a marginal effect on temperature profiles as M varies. This alignment with our comprehension of magnetic phenomena in similar fluid flow scenarios underscores that the presence of a magnetic field has minimal influence on thermal characteristics. Therefore, the first solution more accurately mirrors the natural behaviour observed in systems where magnetic fields exert limited impact on thermal attributes. Conversely, Figure 30(b) delves into the interplay between M and temperature profiles. Here, an increase in the magnetic parameter M corresponds to a proportional increase in temperature profiles.

Figure 31(a) provides insight into the relationship between

the Radiation parameter (R) and fluid velocity, particularly within the context of the first solution. Notably, there is a clear indication that elevating the value of R results in a subsequent increase in fluid velocity. This phenomenon can be attributed to the intensified radiative heat transfer processes. As R increases, the fluid is more receptive to the radiative energy, which in turn stimulates its motion. The heightened fluid velocity in response to elevated R resonates with our understanding of how radiative effects impact fluid dynamics. In contrast, Figure 31(b) sheds light on the influence of R on fluid velocity within the second solution. Surprisingly, despite the radiative nature of R , its increase shows a negligible effect on fluid velocity. This intriguing behaviour might be attributed to the complex interplay of various forces and mechanisms present in the second solution.

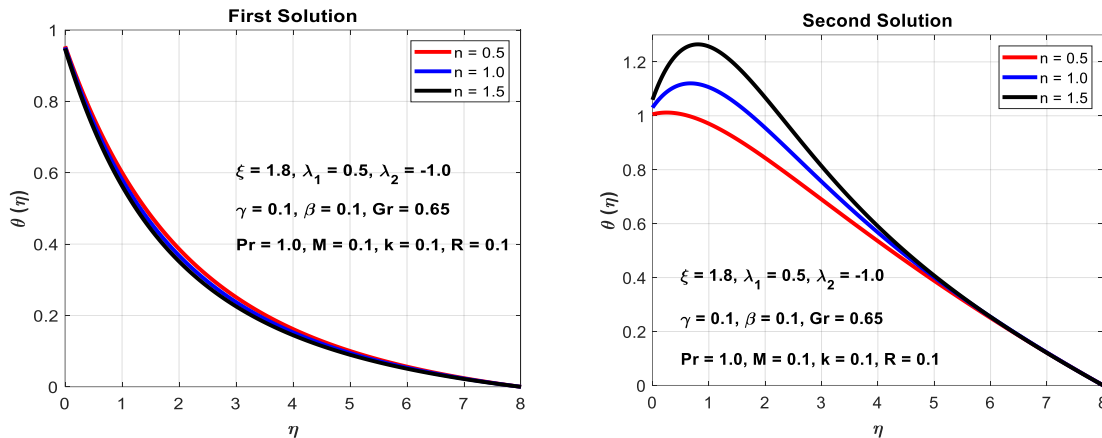


Figure 29. Variation of temperature $\theta(\eta)$ with η with several values of n

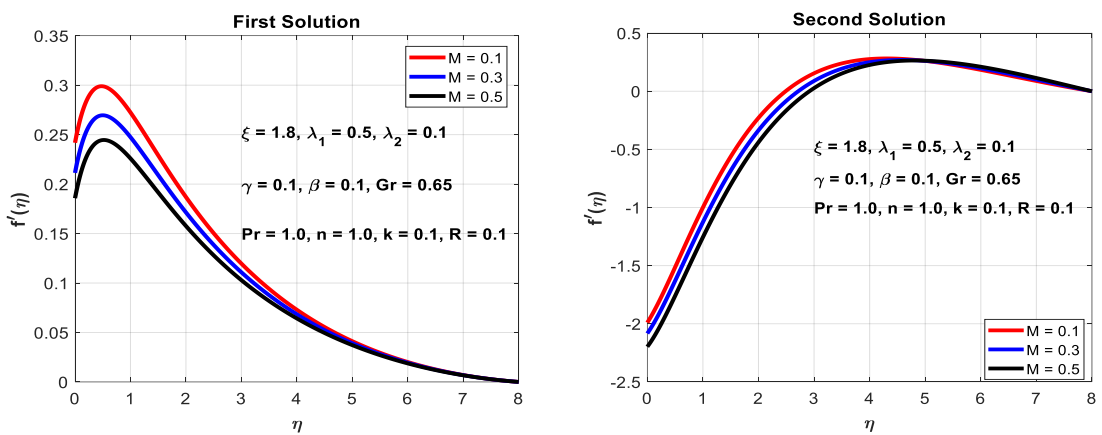


Figure 30. Variation of velocity $f'(\eta)$ with η with several values of M

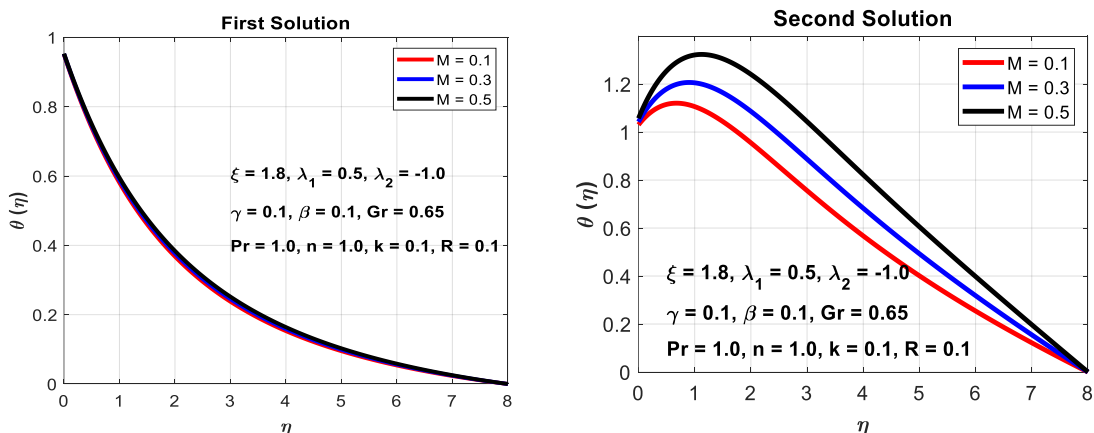


Figure 31. Variation of temperature $\theta(\eta)$ with η with several values of M

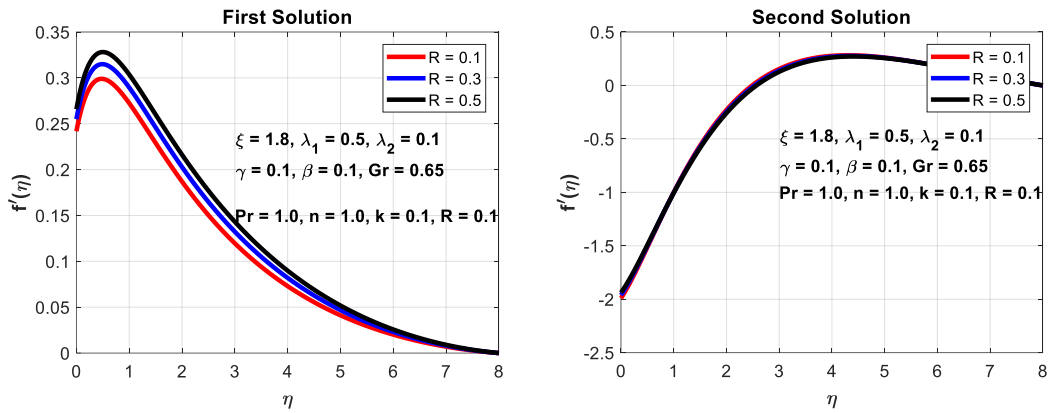


Figure 32. Variation of velocity $f'(\eta)$ with η with several values of R

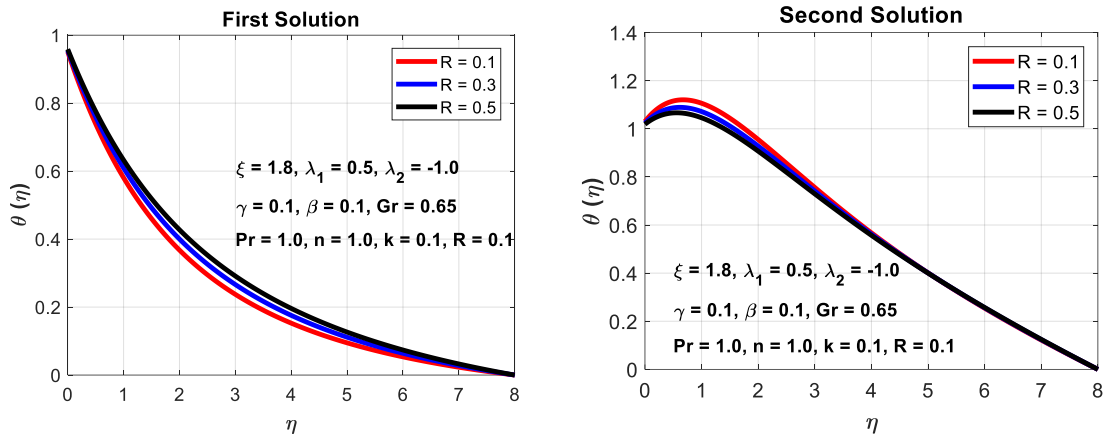


Figure 33. Variation of temperature $\theta(\eta)$ with η with several values of R

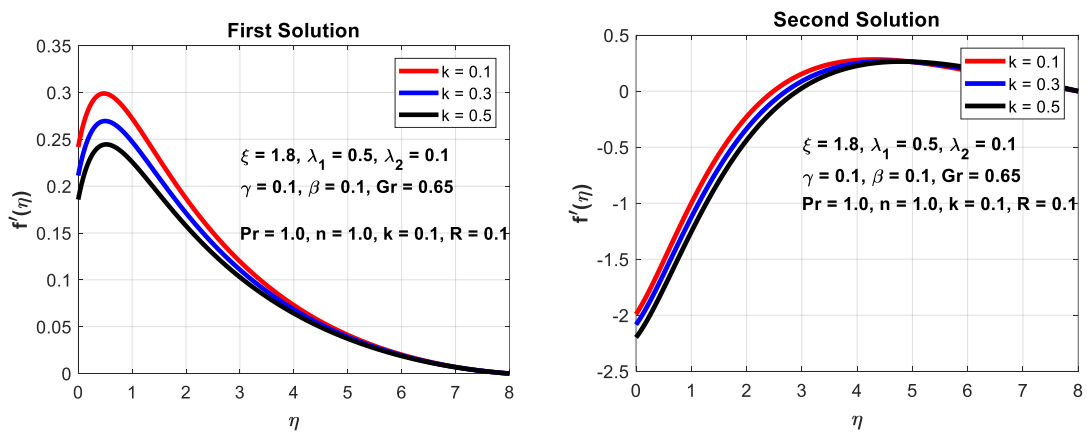


Figure 34. Variation of velocity $f'(\eta)$ with η with several values of k

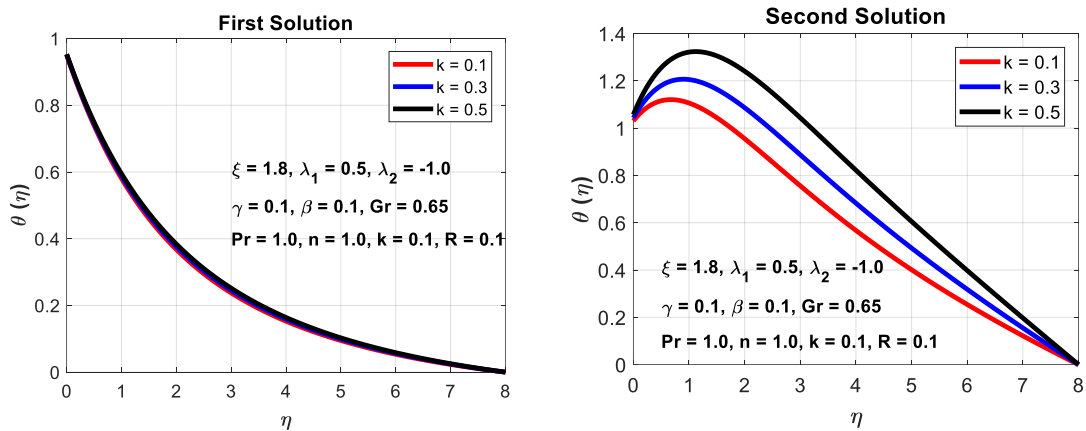


Figure 35. Variation of temperature $\theta(\eta)$ with η with several values of k

Shifting focus to Figure 32(a), we delve into the ramifications of the radiation parameter (R) on fluid temperature distribution. Remarkably, the graph unveils a marginal impact on temperature profiles as R varies. This observation suggests that, in this specific context, radiative effects might not significantly alter the temperature distribution. The marginal variation in temperature profiles as R changes aligns with our understanding of the subtleties involved in radiative heat transfer processes. Conversely, Figure 32(b) delves into the intricate relationship between R and temperature profiles. Here, an increase in the radiation parameter R corresponds to a reduction in temperature profiles. This behaviour resonates with the concept that heightened radiative effects can lead to enhanced heat dissipation and cooling, thereby causing a decrease in temperature. These findings collectively emphasize the nuanced interplay between radiation effects, fluid velocity, and temperature distribution within the investigated system.

Figure 33 offers valuable insight into the interplay between the permeability of the porous medium (k) and fluid velocity. This relationship is particularly pronounced within the first and second solution contexts. It is discernible that augmenting the value of k leads to a subsequent reduction in fluid velocity for both the first and second solutions. This phenomenon can be attributed to the porous medium's impact on fluid flow. As the permeability of the porous medium increases, the ease with which fluid can flow through it diminishes (Figure 34). Figure 35 delves into the impact of k on fluid temperature. Surprisingly, despite the porous nature of k , its increase exhibits a marginal effect on fluid temperature within the first solution. However, in the second solution, an increase in k leads to an augmentation of fluid temperature. This behavior might be due to the varying degrees of interaction between fluid and porous medium, which can influence heat transfer rates differently in distinct solution modes.

5. CONCLUSIONS

The research focused on investigating the intricate dynamics of MHD heat transfer in radiative fluid flow along a stretching cylinder embedded in a porous medium, with a specific emphasis on the impact of second-order slip effects. Through a comprehensive analysis of various parameters and their interactions, significant insights were gained regarding the behavior of fluid velocity and temperature profiles. The study's findings provide valuable contributions to the understanding of complex fluid flow phenomena and thermal behavior in the presence of porous media, magnetic fields, and radiative heat transfer.

- Higher λ_1 amplifies fluid velocity near the surface, while its impact on temperature and heat transfer varies, revealing the intricate interplay between slip effects and thermal behavior in both solutions.
- λ_2 's influence on fluid velocity and heat transfer is mode-dependent; it augments velocity in the first solution but leads to complex interactions within the second solution, illustrating the delicate balance between slip effects and fluid dynamics.
- Increasing k hinders fluid motion, reducing velocity, and altering heat transfer interactions. k 's impact on temperature and heat transfer is distinct in each solution, indicating its pivotal role in governing fluid behavior through the porous medium.

- Elevated n intensifies or dampens fluid velocity based on the solution, influencing temperature profiles accordingly. The opposing n -driven responses provide insights into the complex relationship between thermal and fluid dynamics.
- Higher Gr stimulates buoyancy-driven fluid motion in the first solution and dampens it due to competition between buoyancy and slip effects in the second solution. Temperature profiles respond inversely, highlighting the pivotal role of Gr in shaping flow patterns.
- γ' 's impact on fluid velocity and temperature is consistent in both solutions, enhancing them along with the velocity boundary layer thickness. The changing cylinder curvature's intricate role is revealed, affecting fluid behavior near the surface.
- Elevated M suppresses fluid velocity due to Lorentz forces, showing a uniform effect in both solutions. Temperature response varies, minimally affecting it in the first solution and indicating complex force interactions in the second.
- Increased R intensifies fluid velocity in the first solution via enhanced radiative heat transfer. Contrastingly, the second solution displays nuanced velocity and temperature responses, underscoring the intricate role of radiation in heat transfer.
- Higher Pr diminishes fluid velocity and temperature due to altered thermal conductivity and momentum, impacting velocity and thermal boundary layers near the surface in both solutions.

The study has provided valuable insights into the complex dynamics of heat transfer, with a specific focus on second-order slip effects. However, it is crucial to address the emergence of dual solutions observed in the analysis. The presence of dual solutions introduces uncertainty into the numerical simulations, potentially impacting the accuracy and reliability of the results. To mitigate this uncertainty and ensure the robustness of our findings, further investigations are warranted. These investigations may include sensitivity analyses, validation studies, and alternative numerical approaches to validate the dual solutions and their implications. By addressing these concerns, we can strengthen the credibility of our research and contribute more effectively to the understanding of complex fluid dynamics phenomena in porous media environments.

The applications of our findings span various sectors, including energy generation, aerospace, electronics, renewable energy, nuclear power, chemical processing, biomedical engineering, environmental modeling, and materials processing. These insights pave the way for improved designs, enhanced efficiency, and safer operations in critical industries, thereby contributing to the advancement of science and technology.

REFERENCES

- [1] Ganesan, P., Loganathan, P. (2002). Radiation and mass transfer effects on flow of an incompressible viscous fluid past a moving vertical cylinder. *International Journal of Heat and Mass Transfer*, 45(21): 4281-4288. [https://doi.org/10.1016/S0017-9310\(02\)00140-0](https://doi.org/10.1016/S0017-9310(02)00140-0)
- [2] Ishak, A., Nazar, R., Pop, I. (2008). Magnetohydrodynamic (MHD) flow and heat transfer

- due to a stretching cylinder. *Energy Conversion and Management*, 49(11): 3265-3269. <https://doi.org/10.1016/j.enconman.2007.11.013>
- [3] Chamkha, A.J. (2011). Heat and mass transfer from MHD flow over a moving permeable cylinder with heat generation or absorption and chemical reaction. *Communications in Numerical Analysis*, 2011: 1-20. <https://doi.org/10.5899/2011/cna-00109>
- [4] Makanda, G., Shaw, S., Sibanda, P. (2015). Effects of radiation on MHD free convection of a Casson fluid from a horizontal circular cylinder with partial slip in non-Darcy porous medium with viscous dissipation. *Boundary Value Problems*, 2015: 75. <https://doi.org/10.1186/s13661-015-0333-5>
- [5] Malik, M.Y., Salahuddin, T. (2015). Numerical solution of MHD stagnation point flow of Williamson fluid model over a stretching cylinder. *International Journal of Nonlinear Sciences and Numerical Simulation*, 16(3-4): 161-164. <https://doi.org/10.1515/ijnsns-2014-0035>
- [6] Hayat, T., Tamoor, M., Khan, M.I., Alsaedi, A. (2016). Numerical simulation for nonlinear radiative flow by convective cylinder. *Results in Physics*, 6: 1031-1035. <https://doi.org/10.1016/j.rinp.2016.11.026>
- [7] Mondal, H., Das, S., Kundu, P.K. (2020). Influence of an inclined stretching cylinder over MHD mixed convective nanofluid flow due to chemical reaction and viscous dissipation. *Heat Transfer*, 49(4): 2183-2193. <https://doi.org/10.1002/hjt.21714>
- [8] Yih, K.A. (1999). Radiation effect on natural convection over a vertical cylinder embedded in porous media. *International Communications in Heat and Mass Transfer*, 26(2): 259-267. [https://doi.org/10.1016/S0735-1933\(99\)00012-3](https://doi.org/10.1016/S0735-1933(99)00012-3)
- [9] Soid, S.K., Mohd Gazali, N.H., Yusof, Z.M., Ali, Z.M., Abd Aziz, A.S., Kechil, S.A. (2013). Radiation effects on laminar boundary layer flow along a stretching cylinder. *AIP Conference Proceedings*, 1557: 186-190. <https://doi.org/10.1063/1.4823900>
- [10] Najib, N., Bachok, N. (2022). Numerical analysis of boundary layer flow and heat transfer over a shrinking cylinder. *CFD Letters*, 14(5): 56-67. <https://doi.org/10.37934/cfdl.14.5.5667>
- [11] Chauhan, D.S., Rastogi, P., Agrawal, R. (2014). Magneto hydrodynamic flow and heat transfer in a porous medium along a stretching cylinder with radiation: Homotopy analysis method. *Afrika Matematika*, 25(1): 115-134. <https://doi.org/10.1007/s13370-012-0102-x>
- [12] Pandey, A.K., Kumar, M. (2017). Natural convection and thermal radiation influence on nanofluid flow over a stretching cylinder in a porous medium with viscous dissipation. *Alexandria Engineering Journal*, 56(1): 55-62. <https://doi.org/10.1016/j.aej.2016.08.035>
- [13] Shojaei, A., Amiri, A.J., Ardahaie, S.S., Hosseinzadeh, K., Ganji, D.D. (2019). Hydrothermal analysis of Non-Newtonian second grade fluid flow on radiative stretching cylinder with Soret and Dufour effects. *Case Studies in Thermal Engineering*, 13: 100384. <https://doi.org/10.1016/j.csite.2018.100384>
- [14] Lim, Y.J., Shafie, S., Isa, S.M., Rawi, N.A., Mohamad, A.Q. (2022). Impact of chemical reaction, thermal radiation and porosity on free convection Carreau fluid flow towards a stretching cylinder. *Alexandria Engineering Journal*, 61(6): 4701-4717. <https://doi.org/10.1016/j.aej.2021.10.023>
- [15] Abbas, N., Shatanawi, W., Shatanawi, T.A.M. (2023). Thermodynamic study of radiative chemically reactive flow of induced MHD Sutterby nanofluid over a nonlinear stretching cylinder. *Alexandria Engineering Journal*, 70: 179-189. <https://doi.org/10.1016/j.aej.2023.02.038>
- [16] Jarwal, V.K., Choudhary, S., Sinha, S. (2023). Mixed convection boundary layer nanofluid flow over an inclined stretching cylinder with thermal. *International Journal of Drug Development and Research*, 13(3): 61935-61944. <https://doi.org/10.37118/ijdr.26371.03.2023>
- [17] Wang, C.Y., Ng, C.O. (2011). Slip flow due to a stretching cylinder. *International Journal of Non-Linear Mechanics*, 46(9): 1191-1194. <https://doi.org/10.1016/j.ijnonlinmec.2011.05.014>
- [18] Fang, T., Yao, S., Zhang, J., Aziz, A. (2010). Viscous flow over a shrinking sheet with a second order slip flow model. *Communications in Nonlinear Science and Numerical Simulation*, 15(7): 1831-1842. <https://doi.org/10.1016/j.cnsns.2009.07.017>
- [19] Zhu, J., Zheng, L., Zhang, X. (2011). Hydrodynamic plane and axisymmetric slip stagnation-point flow with thermal radiation and temperature jump. *Journal of Mechanical Science and Technology*, 25(7): 1837-1844. <https://doi.org/10.1007/s12206-011-0423-y>
- [20] Mukhopadhyay, S. (2013). MHD boundary layer slip flow along a stretching cylinder. *Ain Shams Engineering Journal*, 4(2): 317-324. <https://doi.org/10.1016/j.asej.2012.07.003>
- [21] Mishra, U., Singh, G. (2014). Dual solutions of mixed convection flow with momentum and thermal slip flow over a permeable shrinking cylinder. *Computers & Fluids*, 93: 107-115. <https://doi.org/10.1016/j.compfluid.2014.01.012>
- [22] Dhanai, R., Rana, P., Kumar, L. (2016). MHD mixed convection nanofluid flow and heat transfer over an inclined cylinder due to velocity and thermal slip effects: Buongiorno's model. *Powder Technology*, 288: 140-150. <https://doi.org/10.1016/j.powtec.2015.11.004>
- [23] Jain, S., Bohra, S. (2018). Entropy generation on MHD slip flow over a stretching cylinder with heat generation/absorption. *International Journal of Applied Mechanics and Engineering*, 23(2): 413-428. <https://doi.org/10.2478/ijame-2018-0024>
- [24] Soomro, F.A., Zaib, A., Haq, R.U., Sheikholeslami, M. (2019). Dual nature solution of water functionalized copper nanoparticles along a permeable shrinking cylinder: FDM approach. *International Journal of Heat and Mass Transfer*, 129: 1242-1249. <https://doi.org/10.1016/j.ijheatmasstransfer.2018.10.051>
- [25] Mukhopadhyay, S. (2012). Mixed convection boundary layer flow along a stretching cylinder in porous medium. *Journal of Petroleum Science and Engineering*, 96-97: 73-78. <https://doi.org/10.1016/j.petrol.2012.08.006>
- [26] Rashad, A.M., Chamkha, A.J., Modather, M. (2013). Mixed convection boundary-layer flow past a horizontal circular cylinder embedded in a porous medium filled with a nanofluid under convective boundary condition. *Computers & Fluids*, 86: 380-388. <https://doi.org/10.1016/j.compfluid.2013.07.030>
- [27] EL-Kabeir, S.M., Chamkha, A.J., Rashad, A.M. (2014). Effect of thermal radiation on non-Darcy natural convection from a vertical cylinder embedded in a

- nanofluid porous media. *Journal of Porous Media*, 17(3): 269-278. <http://doi.org/10.1615/JPorMedia.v17.i3.70>
- [28] Yadav, R.S., Sharma, P.R. (2014). Effects of porous medium on MHD fluid flow along a stretching cylinder. *Annals of Pure and Applied Mathematics*, 6(1): 104-113.
- [29] Manjunatha, P.T., Giresha, B.J., Prasannakumara, B.C. (2017). Effect of radiation on flow and heat transfer of MHD dusty fluid over a stretching cylinder embedded in a porous medium in presence of heat source. *International Journal of Applied and Computational Mathematics*, 3: 293-310. <http://doi.org/10.1007/s40819-015-0107-x>
- [30] Alizadeh, R., Karimi, N., Arjmandzadeh, R., Mehdizadeh, A. (2019). Mixed convection and thermodynamic irreversibilities in MHD nanofluid stagnation-point flows over a cylinder embedded in porous media. *Journal of Thermal Analysis and Calorimetry*, 135: 489-506. <http://doi.org/10.1007/s10973-018-7071-8>
- [31] Dharmendar Reddy, Y., Goud, B.S., Nisar, K.S., Alshahrani, B., Mahmoud, M., Park, C. (2023). Heat absorption/generation effect on MHD heat transfer fluid flow along a stretching cylinder with a porous medium. *Alexandria Engineering Journal*, 64: 659-666. <http://doi.org/10.1016/j.aej.2022.08.049>
- [32] Merkin, J.H., Najib, N., Bachok, N., Ishak, A., Pop, I. (2017). Stagnation-point flow and heat transfer over an exponentially stretching/shrinking cylinder. *Journal of the Taiwan Institute of Chemical Engineers*, 74: 65-72. <http://doi.org/10.1016/j.jtice.2017.02.008>
- [33] Awaludin, I.S., Ahmad, R., Ishak, A. (2020). On the stability of the flow over a shrinking cylinder with prescribed surface heat flux. *Propulsion and Power Research*, 9(2): 181-187. <http://doi.org/10.1016/j.jprr.2020.03.001>
- [34] Najib, N., Bachok, N., Arifin, N.M., Ishak, A. (2014). Stagnation point flow and mass transfer with chemical reaction past a stretching/shrinking cylinder. *Scientific Reports*, 4: 4178. <http://doi.org/10.1038/srep04178>
- [35] Rai, P., Mishra, U. (2022). Numerical simulation of boundary layer flow over a moving plate in the presence of magnetic field and slip condition. *Journal of Advanced Research in Fluid Mechanics and Thermal Sciences*, 95(2): 120-136. <http://doi.org/10.37934/arfmts.95.2.120136>
- [36] Rai, P., Mishra, U. (2023). Unveiling the behavior of MHD mixed convective nanofluid slip flow over a moving vertical plate with radiation, chemical reaction, and viscous dissipation. *CFD Letters*, 15(10): 93-109. <http://doi.org/10.37934/cfdl.15.10.93109>
- [37] Rai, P., Mishra, U. (2024). Evaluation of combined effect of zero flux and convective boundary conditions on magnetohydrodynamic boundary-layer flow of nanofluid over moving surface using Buongiorno's model. *Engineering Proceedings*, 59(1): 245. <http://doi.org/10.3390/engproc2023059245>